In-depth mass-spectrometry reveals phospho-RAB12 as a blood biomarker of G2019S LRRK2-driven Parkinson's

Adriana Cortés,[1,+] Toan K. Phung,[2,+] Lorena de Mena,[3] Alicia Garrido,[3] Jon Infante,[4] Javier Ruíz-Martínez,[5] Miquel À. Galmés-Ordinas,[6] Sophie Glendinning,[2] Jesica Pérez,[3] Ana Roig,[3] Marta Soto,[3] Marina Cosgaya,[3] Valeria Ravasi,[3] Manel Fernández,[3] Alejandro Rubiano-Castro,[3] Ramón Díaz,[1] Haizea Hernández-Eguiazu,[5] Coro Sánchez-Quintana,[4] Ana Vinagre-Aragón,[5] Elisabet Mondragón,[5] Ioana Croitoru,[5] María Rivera-Sánchez,[4] Andrea Corrales-Pardo,[4] María Sierra,[4] Eduardo Tolosa,[3] Cristina Malagelada,[8] Raja S. Nirujogi,[2] Joaquín Fernández-Irigoyen,[1] Enrique Santamaría,[1] Dario R. Alessi,[2] María J. Martí,[3] Mario Ezquerra,[3,‡,*] Rubén Fernández-Santiago,[3,‡,*]

[1] Proteored-ISCIII, Proteomics Platform, Clinical Neuroproteomics Unit, Navarrabiomed, Departamento de Salud, UPNA, IdiSNA, ES 31008 Pamplona, Spain. [2] Medical Research Council Protein Phosphorylation and Ubiquitylation Unit, University of Dundee, DD1 5EH Dundee, UK. [3] Lab of Parkinson's & Other Movement Disorders, Institut d'Investigacions Biomèdiques August Pi i Sunyer (IDIBAPS); Parkinson's Disease and Movement Disorders Unit, Neurology Service, Hospital Clínic de Barcelona; Institut de Neurociències, Universitat de Barcelona; Centro de Investigación Biomédica en Red sobre Enfermedades Neurodegenerativas (CIBERNED) CB06/05/0018-ISCIII; ES 08036 Barcelona, Spain. [4] Neurology Service, University Hospital Marqués de Valdecilla-IDIVAL; Centro de Investigación Biomédica en Red sobre Enfermedades Neurodegenerativas (CIBERNED); ES 39008 Santander, Spain. [5] Department of Neurology, Donostia University Hospital; Biogipuzkoa Health Research Institute; Centro de Investigación Biomédica en Red sobre Enfermedades Neurodegenerativas (CIBERNED); San Sebastián ES 20014, Spain. [6] In Silico Medicinal Chemistry, Division of Cancer Therapeutics, The Institute of Cancer Research, SW7 3RP London, UK. [7] The Michael J. Fox Foundation for Parkinson's Research, Grand Central Station, P.O. Box 4777, NY 10120 New York, USA. [8] Department of Biomedicine, Faculty of Medicine, Universitat de Barcelona; Institut de Neurociències, Universitat de Barcelona; Centro de Investigación Biomédica en Red sobre Enfermedades Neurodegenerativas (CIBERNED); ES 08036 Barcelona, Spain. ([+]) joint first authors; ([‡]) joint senior authors; (*) Corresponding authors. R. Fernández-Santiago (ruben.fernandez.santiago@gmail.com) & M. Ezquerra (ezquerra@recerca.clinic.cat)

Word count: 6,930

Abstract: 276

Tables and/or figures: 1 Tables / 6 Figures

Supplemental data: 2 Suppl. Tables / 7 Suppl. Figures

References: 85

Characters in the title: 93

Characters in the running title: 69

RUNNING TITLE

Mass-spectrometry of a LRRK2 clinical cohort identifies pSer106 RAB12

KEYWORDS

Parkinson's disease (PD)

Leucine-rich repeat kinase 2 (LRRK2)

Peripheral blood mononuclear cells (PBMCs)

Phospho-/proteomics

Non-manifesting carriers

Biomarker

FINANCIAL DISCLOSURE / CONFLICTS OF INTEREST

No conflicts of interest to declare

ABSTRACT

Leucine-rich repeat kinase 2 (LRRK2) inhibition is a promising disease-modifying therapy for LRRK2-associated Parkinson's disease (L2PD) and idiopathic PD (iPD). Yet, pharmaco-dynamic readouts and progression biomarkers for disease modification clinical trials are insufficient. Employing phospho-/proteomic analyses we assessed the impact that LRRK2 activating mutations had in peripheral blood mononuclear cells (PBMCs) from a LRRK2 clinical cohort from Spain (n=174) encompassing G2019S L2PD patients (n=37), non-manifesting LRRK2 mutation carriers of G2019S, here, G2019S L2NMCs (n=27), R1441G L2PD patients (n=14), R1441G L2NMCs (n=11), iPD (n=40), and controls (n=45). We identified 207 differential proteins in G2019S L2PD compared to controls (39 up/ 168 down) and 67 in G2019S L2NMCs (10 up/ 57 down). G2019S down-regulated proteins affected the endolysosomal pathway, proteostasis and mitochondria, e.g., ATIC, RAB9A, or LAMP1. At the phospho-proteome level, we observed increases in endogenous phosphorylation levels of pSer106 RAB12 in G2019S carriers, which were validated by immunoblotting after 1 year of follow-up (n=48). Freshly collected PBMCs from 3 G2019S L2PD, 1 R1441G L2PD, 1 iPD, and 5 controls (n=10) showed strong diminishment of pSer106 RAB12 phosphorylation levels after in-vitro administration of the MLi-2 LRRK2 inhibitor. Using machine learning, we identified an 18-feature G2019S phospho-/protein signature capable of discriminating G2019S L2PD, L2NMCs, and controls with 96% accuracy that correlated with disease severity, i.e., UPDRS-III motor scoring. Our study identified pSer106 RAB12 as an endogenous biomarker in easily accessible PBMCs from G2019S carriers and suggests that phospho-/proteomic findings in human PBMCs such as pSer106 RAB12 can be deployed as a universal pharmaco-dynamic readout for L2PD, L2NMCs, and iPD. Future work may determine whether pSer106 RAB12 could help with patient enrichment and monitoring drug efficacy in LRRK2 clinical trials.

ABBREVIATIONS

(Minimal abbreviations to be used in the text)

PBMCs = Peripheral blood mononuclear cells

CNS = Central nervous system

DIA = Data independent acquisition

MS = Mass-spectrometry

PD = Parkinson's disease

LRRK2 = Leucine-rich repeat kinase 2

L2PD = LRRK2-associated PD patients

L2NMCs = Non-manifesting LRRK2 mutation carriers

iPD = Idiopathic PD patients

p = Phospho-

FC = Fold-change

INTRODUCTION

Activating mutations in the leucine-rich repeat kinase 2 (*LRRK2*), e.g., G2019S or R1441G, increase LRRK2 kinase activity[1–4] causing autosomal-dominant LRRK2 Parkinson's (L2PD).[5,6] By converging pathways, LRRK2 kinase activity appears to be also enhanced in patients with idiopathic PD (iPD),[7–9] undistinguishable from L2PD at the clinical level.[10,11] Thus, ongoing clinical trials of small-molecule type-I inhibitors targeting active LRRK2 protein conformation is a promising disease-modifying strategy for a broad spectrum of patients.[12,13] Moreover, non-manifesting LRRK2 mutation carriers (L2NMCs) are at high risk of PD in an age-dependent progressive manner,[14–16] representing a candidate population for the continued clinical follow-up and disease course modification by early neuroprotective interventions when needed.[13]

A subset of G-proteins from the Ras-related small GTPase superfamily[17] was reported as phosphorylation substrates of the LRRK2 Ser/Thr kinase.[2,3] Among these, pThr73 RAB10 was validated as a LRRK2 substrate[18] showing elevated phosphorylation levels in a large set of R1441G carriers, symptomatic and asymptomatic, yet not in G2019S,[19] and also a readout for LRRK2 pharmacological inhibition using Mli-2 or DNL201.[20,21] Moreover, RAB29[22,23] and more recently RAB12[24,25] and RAB32[26] have been described as key upstream LRRK2 activators. Despite significant progress, we still lack robust pharmaco-dynamic readouts and clinical progression biomarkers useful in disease modification clinical trials.

Employing data-independent acquisition (DIA) mass-spectrometry (MS), we have screened the phospho-/proteome of PBMCs from a LRRK2 clinical cohort (n=174) of G2019S L2PD (n=37), G2019S L2NMCs (n=27), R1441G L2PD (n=14), R1441G L2NMCs (n=11), iPD (n=40), and controls (n=45). We identified differential phospho-/proteins in G2019S and R1441G carriers, symptomatic and asymptomatic. We found elevated levels of pSer106 RAB12 phosphorylation in G2019S carriers. Our results suggest that pSer106 RAB12 comprises an endogenous biomarker in G2019S PBMCs, as it is similarly elevated in both L2PD and L2NMCs. Consistent with RAB12 being phosphorylated by LRRK2 we found that pSer106 RAB12 levels strongly diminished after Mli-2 LRRK2 inhibition in all subjects, regardless of their disease or mutation status. We propose that pSer106 RAB12 could be exploited as a target engagement biomarker in LRRK2 clinical trials.[13] We provide full open access to all data generated here through FAIR,[27] and Curtain[28].

METHODS

Subjects

Probands participated in the study after local ethics approval and signed informed consent. Study subjects included LRRK2 mutation carriers, symptomatic and asymptomatic, iPD patients, and healthy controls including healthy spouses and companions of Spanish descent. Patient inclusion criteria were a clinical diagnosis of PD by a movement disorders specialist based on the MDS clinical diagnostic criteria for Parkinson's.[29] Exclusion criteria were chronic inflammatory and autoimmune diseases, e.g., Crohn's (CD), inflammatory bowel disease (IBD), rheumatoid arthritis, systemic lupus erythematosus (SLE); chronic neurological diseases such as myasthenia gravis, chronic use of nonsteroidal anti-inflammatory drugs (NSAIDs) or corticosteroid anti-inflammatory medication, and viral or bacterial infection during the week precedent to blood sample donation. Subjects were recruited at three centres from Spain, Hospital Clínic de Barcelona (n=76) ('B'),[30] Hospital Marqués de Valdecilla in Santander (n=55) ('S'),[31] and Hospital de Donostia in San Sebastian (n=43) ('D')[32] (**Table 1**). By cohort and subject type, the sample included G2019S L2PD (n=37) (16 from B, 20 from S, and 1 from D), G2019S L2NMCs (n=27) (11 B, 15 S, and 1 D), R1441G L2PD (n=14) (1 B, and 13 D), R1441G L2NMCs (n=11) (3 B, and 8 D), iPD (n=40) (20 B, 10 S, and 10 D), and controls (n=45) (25 B, 10 S, and 10 D). We also collected gender, age at sampling, age-at-onset (AAO), LRRK2 mutation status, kinship to index cases, UPDRS-III,[33] MoCA,[34] autoimmune and environmental structured questionnaires, COVID-19 history. Specifically, PD patients had a mean age-at-sampling of 63.5 years for G2019S L2PD, 67.1 for R1441G L2PD, and 67.3 for iPD. Asymptomatic blood relatives of L2PD patients, i.e., L2NMCs, were younger than PD patients with a mean age of 56.7 years for G2019S L2NMCs and 61.1 for R1441G L2NMCs. The AAO was similar for G2019S and R1441G L2PD with 55.1 and 55.8 years respectively, whereas iPD had 62.1 years on average. Mean disease duration was 8.4 years for G2019S L2PD, 12.3 for R1441G L2PD and 5.2 for iPD. Average disease severity, UPDRS-III motor scoring, was similar (mild) in all three patient groups, i.e., 16.0 in G2019S L2PD, 19.8 R1441G L2PD, and 19.7 for iPD. Mean MoCA scores were also mild and similar in all patients, 24.3 for G2019S L2PD, 23.2 for R1441G L2PD, and 25.6 for iPD. As for medication, L-DOPA equivalent daily dose (LEDD) was 635.8 mg for G2019S L2PD, 711.5 mg for R1441G L2PD, and 584.7 mg for iPD.

Genotyping

We genotyped the most common LRRK2 mutations in our population using Taqman SNP assays-on-demand for *LRRK2* G2019S (Thermo Fisher Sci., #C-63498123-10) and a commercial TaqMan assay for *LRRK2* R1441G[35] on a Step One Plus Real-time PCR System (Life Tech. Inc.)

PBMC isolation

40 ml of peripheral blood were drawn early in the morning in fasting and PBMCs were isolated by density gradient using Sodium-Citrate tubes (BD Vacutainer CPT, #EAN30382903627821) following manufacturer's instructions. All samples used in the study were dry PBMC pellets flash-frozen in liquid N_2 and stored at -80°C for a time period less than a year until use.

PBMC preparation

PBMC samples from the three cohorts were processed in parallel. Blind experimental groups to the operator were balanced and randomized in runs to avoid manipulation bias. Briefly, PBMCs were homogenized in lysis buffer (7 M urea, 2 M thiourea, 50 mM dithiothreitol) and supplemented with cOmplete Mini protease (Roche, #11836153001) and PhosSTOP phosphatase (Roche, #4906845001) inhibitors. Lysates were centrifuged at 20,000g, 1h, 15°C, and the resulting supernatant was quantified by the Bradford assay (Bio-Rad, #5000201). To obtain phosphorylated fractions, above 400 µg of protein were separated for protein digestion. Proteins were reduced with DTT (final concentration of 20 mM; 30 min; room temperature), alkylated with iodoacetamide (final concentration of 30 mM; 30 min in dark; room temperature), diluted to 0.9 M with ABC, and digested with trypsin (Promega, #V5280) (1:20 w/w enzyme protein ratio, 18h, 37°C). Protein digestion was interrupted by acidification (acetic acid, pH<6), and the resulting peptides were cleaned up using Pierce Peptide Desalting Spin Columns (Thermo Fisher Sci., #89851). Phospho-peptide enrichment was performed using the High-Select TiO_2 Phospho-peptide enrichment Kit (Thermo Fisher Sci., #A32993) according to the manufacturer's instructions. Lastly, the enriched phospho-enriched fractions were cleaned up as described above and dried-down in a Speed Vacuum system. Aliquots of 10 µg cleaned up peptides from protein digestions were set aside for total protein analyses.

Data independent acquisition (DIA) mass-spectrometry (MS)

Dried-down peptide samples were reconstituted with 2% ACN-0.1% FA (Acetonitrile-Formic acid), spiked with internal retention time peptide standards (iRT, Biognosys), and quantified by NanoDropTM spectrophometer (ThermoFisher Sci.) before LC-MS/MS in an EASY-1000 nanoLC system coupled to an EZ-Exploris 480 mass spectrometer (Thermo Fisher Sci.). Peptides were resolved using C18 Aurora column (75µm x 25cm, 1.6 µm particles; IonOpticks) at a flow rate of 300 nL/min using a 60-min gradient (50°C): 2% to 5% B in 1 min, 5% to 20% B in 48 min, 20% to 32% B in 12 min, and 32% to 95% B in 1 min (A = FA, 0.1%; B = 100% ACN:0.1% FA). Peptides were ionized using 1.6 kV spray voltage at a capillary temperature of 275 °C. We used data-independent acquisition (DIA) with full MS scans (scan range: 400 to 900 m/z; resolution: 60,000; maximum injection time: 22 ms; normalised AGC target: 300%) and 24 periodical MS/MS segments applying 20 Th isolation windows (0.5 Th overlap: Resolution: 15000; maximum injection time: 22 ms; normalised AGC target: 100%). Peptides were fragmented using a normalized HCD collision energy of 30%. MS data files were analysed using Spectronaut (Biognosys) by direct DIA analysis (dDIA). MS/MS spectra were searched against the Uniprot proteome reference from the *Homo sapiens* database UP000005640 using standard settings. The enzyme was set to trypsin in a specific mode. On the one hand, Carbamidomethyl (C) was set as a fixed modification, and oxidation (M), acetyl (protein N-term), deamidation (N), and Gln to pyroGlu as variable modifications for total protein analysis. On the other hand, Carbamidomethyl (C) was set as a fixed modification, and oxidation (M), acetyl (protein N-term), and Phospho (STY) as variable modifications for phospho-proteome analysis. Identifications were filtered by a 1% Q-value. After MS, samples that did not pass QC were omitted from the study, resulting in a sample of G2019S L2PD (n=32) (15 from B and 17 from S), G2019S L2NMCs (n=22) (9 B and 13 S), R1441G L2PD (n=13) (1 B, and 12 D), R1441G L2NMCs (n=7) (2 B, and 5 D), iPD patients (n=39) (19 B, 10 S, and 10 D), and healthy controls (n=42) (23 B, 10 S, and 9 D). Lastly, to disambiguate peptide IDs into gene names we used the Uniprot online database (https://uniprotparser.proteo.info/).

Proteome differential analysis

Proteome MS output data was exported from .SNE files from Spectronaut in a pivot table text format. For the differential analyses between groups, MS data was processed using QFeatures (doi: 10.18129/B9.bioc.QFeatures) in R (QFeatures v1.13.1). We applied the following R workflow: (i) Data was filtered to remove proteins identified by only 1 peptide sequence. (ii) Data selection was done based on condition and sub-group labels, with overall analysis containing all samples, G2019S analyses containing Barcelona and Santander samples labelled with prefix "B" or "S", and R1441G analyses containing samples labelled with prefix "D" from Donostia-San Sebastian and "B" from Barcelona if bearing R1441G. For each analysis, we provided a separate Rscript file with a customized group selection (**Suppl. Material**). (iii) A protein ID column was assigned as an identification column for the analysis with QFeatures. (iv) We filtered out any row with 70% or more missing data. Here, with a 70% missing data cut-off, a meta-analysis would have a total of 3,815 rows while a more common 30% missing data cut-off would result in 3,789 rows. Since there was only about a 0.71% difference between the cut-off threshold, we chose the 70% cut-off so that we could keep entries potentially found in only one group without affecting the statistical power of the entire analysis. (v) Imputation of missing data was done using the kNN method (QFeatures v1.13.1). Subsequently, (vi) we performed a log2 transformation of the imputed data matrix, and (vii) designed a contrast matrix for differential analysis using limma.[36] (viii) For each contrast matrix, we performed a limma analysis with false discovery rate (FDR) Benjamini & Hochberg (BH) multiple testing adjustment and collected the outputs under the criteria for statistical significance of an FDR-BH adjusted $P<0.05$ (1.12 log10) and a $\log_2$ fold-change (FC) above $|0.6|$ ($|1.5|$ in lineal values). Scripts for proteome raw data download and re-analysis are available online (**Suppl. Material**). For ANOVA analysis, we used the normalized data from above as starting point. The data from each row was grouped depending on the criteria used for grouping. Then for each comparison, we applied a Python script using one-way ANOVA analysis on the grouped data within the comparison and returned the P-value output as a new column.[37] Then we perform the same FDR-BH correction from above to obtain the multiple testing adjusted P-values using the Statsmodels Python package[38] with Python scripts also available online (**Suppl. Material**).

Phospho-proteome differential analysis

Phospho-proteome MS data was exported from .SNE files from Spectronaut in a long-form table format using a Spectronaut param export file available online (**Suppl. Material**). Data was imputed using a modified version of a collapsing R script (Perseus Plugin Peptide Collapse)[39] with phosphorylation as target modification at a confidence cut-off above 0.75. Modified collapsing.R and Perseus parameter.xml files are available online (**Suppl. Material**). We applied the following R workflow: (i) Columns with more than 70% blank cells were removed to meet the kNN requirement of less than 80% blank columns. (ii) Data selection for QFeatures input was based on condition and sub-group labels using all samples for overall analysis or specific group combination for location-specific and mutation-specific group combination, with overall analysis containing all samples, G2019S analyses containing Barcelona and Santander samples labelled with prefix "B" or "S", and R1441G analyses containing samples labelled with prefix "D" from Donostia-San Sebastian and "B" from Barcelona when carrying R1441G. For each phospho-analysis group, we provide a separate Rscript file with customization to the selection group (**Suppl. Material**). Subsequently, (iii) we performed imputation by removing any row with 30% or more empty data similar to the proteome analysis using the kNN method, and (vi) performed log2 transformation normalization of the data using the quantile normalization method. (v) The statistical significance criteria were set at an FDR-BH adjusted $P<0.05$ (1.12 in $\log_{10}$) and a $\log_2$ fold-change (FC) above |0.6| (|1.5| in lineal values). (vii) In each differential analysis, we matched the protein and its original sequence using protein UniProt ID and performed the extraction of PTM position in protein and peptide, the peptide sequence, and the sequence window for visualization at the Curtain tool.[28] Scripts for phospho-proteome data re-analysis are available online (**Suppl. Material**). For phospho-proteome ANOVA analysis, we followed the same methodology as for the proteome analysis but using the normalized phospho-proteome datasets from above. Data belonging to each group was identified from their column name. One-way ANOVA was applied on each row of cell groups from their respective comparison. The final statistically significant output values were adjusted using the Statsmodels package under the same FDR-BH multiple testing adjustment of $P<0.05$. Python scripts for ANOVA phospho-proteome analyses are also available online (**Suppl. Material**).

Data visualisation

Aligning to FAIR principles[27] of data findability, accessibility, interoperability, and reusability, we used Curtain and Curtain PTM,[28] as free open-source tools for MS phospho-/proteomics data mining and exploitation by MS non-experts. Visualization of each of the differential analysis results from limma was done in volcano plot representation using the default cut-off settings of a fold-change (FC) above |1.5| (|0.6| log2) and a FDR-BH adj. P<0.05 (1.12 in $\log_{10}$). The Curtain tools enable interactively perusing volcano plots, deconvoluting primary experimental data to individual replicates that can be visualized in bar charts or violin plots allowing statistical analysis, and export of plots in .SVG format (Curtain tutorials). For each analysis, we also provide web links in the Figures and Figure legends. From each link, users can view the data associated with each data point on the volcano plot in the form of bar charts and violin plots. The magnitude of the data within these plots represents the relative intensity of the protein (total proteome) or phospho-site (phospho-proteome) before normalization. Beyond simple visualization of the numerical data, Curtain tools also aggregate data for different knowledgebases including UniProt, AlphaFold, PhosphoSitePlus, ProteomicsDB, and StringDB.

Machine learning modelling of G2019S differential phospho-/proteins

The normalized and imputed datasets comprising differentially expressed peptides and phospho-peptides were employed to train a multi-class classifier to distinguish between Controls, G2019S L2PD and G2019S L2NMC. Three distinct candidate models were considered including Support Vector Machine (SVM), Random Forest (RF), and Gradient Boosting (GB) classifiers as described in other studies.[40] Parameter optimization of the models through a grid search with a 5-fold cross-validation. To mitigate potential performance degradation due to unbalanced group sizes, we applied the Synthetic Minority Over-sampling Technique (SMOTE)[41] to the training split. We used the balanced accuracy score[42] defined as the average recall across each class, as a metric to evaluate models performances. Implementation of the models was done using the Scikit-learn[43] v1.3.1 library within Python[44] programming language v3.9.18.

Classifier selection by comparative performance of machine learning models

In the G2019S proteome dataset, we included a total of 32 G2019S L2PD, 22 G2019S L2NMCs, and 42 controls that overpassed the QC criteria described above. Similarly, the phospho-proteome dataset comprised 29 G2019S L2PD, 19 G2019S L2NMCs, and 35 controls. First, we assessed comparative model performances for each dataset considering an initial number of features 3,816 peptides and 10,180 phospho-peptides respectively (**Suppl. Table 1**). Notably, in the proteome dataset, the SVM classifier demonstrated a substantial enhancement in balanced accuracy score following redundant feature elimination, achieving 0.91. This outcome indicates that the selective elimination of features contributed to obtaining a more discriminative model. Contrarily, the RF classifier showed limited improvement, implying that feature elimination methods were less effective for this specific model. Consistently, we obtained similar results for the phospho-proteome dataset where, after feature elimination, SVM achieved a balanced accuracy of 0.95, again highlighting the efficacy of feature selection in enhancing model performance. Furthermore, GB demonstrate significant improvement with only 43 features. This result indicates that the model performance can be enhanced with only a small subset of features. After comparative evaluation and parameter optimization, we identified SVM as the resulting most optimal model to derive informative LRKK2 signatures using the minimum subset of relevant features that maximize the discrimination between classes.

Suppl. Table 1. Detail of the performance of each model across (phospho-)/proteome datasets.

Proteome				
Model	Initial (3,816 features)	ANOVA (926 features)	ANOVA + RFECV	Feature optimal Nr.
SVM	0.69 ± 0.09	0.85 ± 0.08	0.91 ± 0.07	510
RF	0.68 ± 0.09	0.70 ± 0.12	0.67 ± 0.08	536
GB	0.69 ± 0.08	0.82 ± 0.13	0.67 ± 0.09	881
Phospho-proteome				
Model	Initial (10,180 features)	ANOVA (979 features)	ANOVA + RFECV	Feature optimal Nr.
SVM	0.39 ± 0.11	0.79 ± 0.03	0.95 ± 0.07	204
RF	0.41 ± 0.10	0.53 ± 0.03	0.61 ± 0.10	91
GB	0.40 ± 0.08	0.47 ± 0.07	0.81 ± 0.06	43

SVM = Support Vector Machine; RF = Random Forest; GB = Gradient Boosting

Identification of a differential G2019S phospho-/protein signature

After SVM model selection, an initial set of relevant features was determined by incorporating only statistically significant features (P<0.05) identified by ANOVA test. Subsequently, we applied Recursive Feature Elimination with Cross-Validation (RFECV)[45] to iteratively reduce the number of features while maximizing the balanced accuracy score. To obtain the LRKK2 signature, we employed the Monte Carlo Tree Search (MCTS)[46] method. The MCTS strategy involved selecting the minimum combination of features that maximize the score in additive manner. Considering that the combinatorial features scale rapidly, the depth of the tree was fixed to five to manage computational complexity. The reward at each node of the tree was computed as the balanced accuracy score obtained through model training with cross-validation, utilizing the selected subset of features. At each iteration, the number of trees evaluated was set to 10 times the number of features. Following the evaluation of all the trees, the MCTS identified the best feature to add, maximizing the reward. A stop node was introduced to halt the algorithm when no further improvement could be achieved. In summary, the procedure comprised: (i) selection of the first feature, (ii) MTCS evaluation of all possible trees and reward calculation, (iii) selection of the best feature to be added, (iv) iteration from the second step until the model stops, (v) repetition from the first step until all features were screened. After the screening of all features, we selected the combinations of features with a balanced accuracy score above 0.90. The most prominently represented features were used as initial features for refinement by MCTS. Discriminant LRKK2 signatures were defined as the subset with the highest score after the refinement. Feature selection and refinement were implemented in Python v3.9.18 using Scikit-learn v1.3.1 and MCTS v2.0.4 libraries (https://pypi.org/project/monte-carlo-tree-search).

Phospho-/protein gene ontology enrichment

Differential phospho-/proteins gene ontology (GO) was assessed using Metascape[47] cell component term using default settings (min. overlap: 3, min. enrichment: |1.5|, P<0.05), and false discovery rate (FDR) adjusted P<0.05. Specifically, for signature phospho-/proteins, we used a combination of cell component and biological processes, and KEEGs, Reactome and wiki pathways under the same statistical significance cut-off.

pSer106 RAB12 immunoblotting of 1-year follow-up PBMCs

To assess the levels of pSer106 RAB12 and other markers over time we isolated PBMCs using 40 ml of blood from a subset of subjects from Clínic-Barcelona (n=48), collected >1-year after DIA-MS, including G2019S L2PD (n=12), G2019S L2NMCs (n=6), iPD (n=15), and controls (n=15). Cell lysates were mixed with the NuPAGE LDS Sample Buffer (Life Technologies) supplemented 5% (v/v) 2-mercaptoethanol and heated to 90°C for 10 minutes. 10 µg of protein was loaded onto NuPAGE 4–12% Bis-Tris Midi Gels (Thermo Fisher, #WG1403BX10). Following the manufacturer's instructions, samples were electrophoresed in NuPAGE MOPs SDS running buffer (Thermo Fisher). Protein transfer was performed onto nitrocellulose membranes (GE Healthcare, Amersham Protran Supported 0.45 µm NC) at 100 V for 90 min on ice in transfer buffer (48 mM Tris–HCl and 39 mM glycine supplemented with 20% methanol) or through turbotransfer. MLi-2 treated protein extracts were electrophoresed in 4–15% Mini-PROTEAN® TGX™ Precast Protein Gels (Bio-Rad, #4561084) and transfer onto trans-Blot Turbo Mini 0.2 µm Nitrocellulose Transfer (BIORAD, #1704158) through a Trans-Blot Turbo Transfer System (BIORAD) following the manufacturer's instructions. Following transfer, membranes were blocked using 5 (w/v) skim milk dissolved in TBS-T (20 mM Tris–HCl, pH 7.5, 150 mM NaCl, and 0.1% (v/v) Tween 20) at RT, for 30 minutes. Membranes were then washed once with TBS-T before they were incubated overnight at 4°C with primary antibodies diluted in 5% BSA (Sigma) dissolved in TBS-T. Membranes were washed 3x with TBS-T for 5 min each before incubation with secondary antibodies diluted in TBS-T at RT for 1 hour. Following secondary incubation, the membranes were then washed 3x with TBS-T for 10 min each. Acquisition of protein bands was performed with near-infrared fluorescent detection using the Odyssey CLx imaging system and quantified using the Image Studio software. The sheep monoclonal anti-total RAB12 antibody was purified by MRC PPU Reagents and Services at the University of Dundee and was used at a final concentration of 1 µg/ml. Mouse monoclonal anti-GAPDH (Santa Cruz Biotechnology, sc-32233) was used at 1:10,000. In-house generated mouse monoclonal anti-total LRRK2, rabbit monoclonal anti-pSer935 LRRK2 (Abcam, #ab133450), rabbit polyclonal anti-total RAB12 (Protein Tech, #18843-1-AP), rabbit monoclonal anti-pSer106 RAB12 (Abcam, #ab256487), rabbit monoclonal anti-RAB9A (Cell Signalling Technologies, #5118), rabbit monoclonal anti-LAMP1

(Cell Signalling Technologies, #9091), and mouse monoclonal anti-Tubulin (Cell signalling Technologies, #3873S) were used at a 1:1,000 dilution (**Suppl. Table 2**). Secondary antibodies, anti-mouse (Licor, #926-68022), anti-rabbit (Licor, #926-32213), and anti-goat (Licor, #926-68074), which has sheep cross-reactivity, were used at a 1:10,000 dilution.

Suppl. Table 2. Primary antibodies list.

Antibody Description	Company	Cat. Number	Dilution / Concentration
Mouse monoclonal GAPDH (6C5)	Santa Cruz	#sc-32233	1:10,000
Rabbit monoclonal LAMP1 (D2D11)	Cell Signalling Tech.	#9091	1:1,000
Mouse monoclonal Total LRRK2	In house generated	-	1:1,000
Rabbit pSer935 LRRK2 [UDD2 10(12)]	Abcam	#ab133450	1:1,000
Rabbit monoclonal RAB9A (D52G8)	Cell Signalling Tech.	#5118	1:1,000
Mouse monoclonal RAB10	Merck	#SAB5300028	1:1,000
Rabbit recombinant pThr73 RAB10 (MJF-R21)	Abcam	#ab230261	1:1,000
Sheep polyclonal Total RAB12	MRC-PPU Reagents and Services at the University of Dundee	#SA227	1 µg/ml
Rabbit monoclonal pSer106 RAB12 (MJF-R25-9)	Abcam	#ab256487	1:1,000
Mouse monoclonal Tubulin (DM1A)	Cell Signalling Tech	#3873S	1:1,000

pSer106 RAB12 immunoblotting after MLi-2 LRRK2 inhibition in fresh PBMCs

To assess the response of pSer106 RAB12 to MLi-2 LRRK2 inhibition we additionally isolated PBMCs from 40 ml of peripheral blood of an additional set of subjects (n=10), including G2019S L2PD (n=3), R1441G L2PD (n=1), iPD (n=1), and healthy controls (n=5). These cells were collected > 2 years after DIA-MS. Each 20 ml of freshly extracted PBMCs was aliquoted into two technical replicates of two tubes of 5 ml each to perform MLi-2 pharmacological inhibition following the Dundee PBMCs isolation protocol (doi: dx.doi.org/10.17504/protocols.io.bnhxmb7n) (from whole blood). Briefly, each technical replicate was treated with either 200 nM MLi-2 LRRK2 inhibitor or an equivalent volume of DMSO (5 µl) for 30 min at room temperature. Next, treated PBMCs were centrifuged at 355g for 5 min. Each pellet was resuspended in 1 ml of PBS containing

2% FBS with or without 200 nM MLi-2, and transferred into an Eppendorf tube. After centrifugation at 300 g for 3 min, treated PBMC pellets were lysed with 70 µl of ice-cold lysis buffer (50 mM Tris–HCl, pH 7.5, 1% Triton X-100, 1 mM EGTA, 1 mM sodium orthovanadate, 50 mM NaF, 0.1% 2-mercaptoethanol, 10 mM 2-glycerophosphate, 5 mM sodium pyrophosphate, 0.1 µg/ml mycrocystin-LR, 270 mM sucrose, 0.5 mM DIFP and Complete EDTA-free protease inhibitor cocktail) on ice for 10min. Then, treated PBMC cell lysates were centrifuged at 14,000 rpm 15 min at 4°C and supernatant was collected. Protein concentrations were assessed at a 1:15 dilution through the Bradford assay. Protein extracts were immediately used for immunoblotting or snap-frozen and stored at −80°C. Subsequent immunoblot analysis was done as described above, with some specificities: Brielfly, MLi-2 treated protein extracts were electrophoresed in 4–15% Mini-PROTEAN® TGX™ Precast Protein Gels (Bio-Rad, #4561084) and transferred onto trans-Blot Turbo Mini 0.2 µm Nitrocellulose Transfer (Bio-Rad, #1704158) through a Trans-Blot Turbo Transfer System (Bio-Rad) following the manufacturer's instructions. Acquisition of protein bands for MLi-2 protein extracts was performed on LAS4000 system and processed through the BandPeak plugin (doi: dx.doi.org/10.17504/protocols.io.7vghn3w) at the ImageJ software. For this experiment, mouse monoclonal anti-RAB10 (Merck, #SAB5300028), rabbit recombinant anti-pThr73 RAB10 (Abcam, #ab230261), rabbit polyclonal anti-RAB12 (Protein Tech, #18843-1-AP), rabbit monoclonal anti-p106 RAB12 (Abcam, #ab256487) were used at a 1:1,000 dilution (**Suppl. Table 2**). As secondary antibodies we used goat anti-rabbit (ThermoFisher, #31460) and goat anti-mouse (Abcam, #ab205719).

Clinical correlation of LRRK2 differential phospho-/proteins and disease severity

We performed a Spearman's association analysis between the differential proteins and phospho-proteins across different comparisons (log2FC>|0.6|, adj. P<0.05) and UPDRS-III motor scores from PD patients and healthy controls. To this end, we used the "cor.test" function from R (stats v4.3.1) to calculate Rho coefficients and the EnhancedVolcano package (v1.20.0) to represent correlation outputs. Statistical significance was set a Spearman's correlation coefficient Rho>|0.5| and an FDR multiple-testing adjusted P<0.05.

RESULTS

We succeeded in quantifying the levels of 3,798 unique proteins using DIA-MS from a LRRK2 clinical cohort (n=174) (**Fig. 1**). Pairwise analysis, under a cut-off of ≥2 peptide mapping, <0.30 imputation, $log_2FC>|0.60|$, and adj. P<0.05, revealed that G2019S L2PD was the most distinct group displaying a set of 207 proteins whose levels differed vs controls, with 85% down-regulated proteins (168 down/ 39 up) (**Fig. 2**). We found that in G2019S L2PD a number of proteins expression was reduced namely, ATIC, which can repress LRRK2 and rescue neurodegeneration[48] ($log_2FC=-0.97$, adj. $P=1.92x10^{-13}$); RAB9A, involved in phagocytic vesicle trafficking and lysosomal function ($log_2FC=-1.17$, adj. $P=3.97x10^{-10}$); or LAMP1, a lysosome biogenesis and autophagy regulator ($log_2FC=-1.32$, adj. $P=1.63x10^{-9}$). G2019S L2NMCs vs controls showed 67 differential hits, involving mostly down-regulated proteins (57 down/ 10 up), common and with the same FC direction as L2PD (42 of 67), e.g., ATIC or LAMP1 (**Suppl. Fig. 1**). G2019S L2PD vs L2NMCs differed only in 2 proteins down-regulated in G2019S L2PD, RAB9A ($log_2FC=0.77$, adj. P=0.038) and SCLY, a Selenocysteine lyase involved in peptide elongation ($log_2FC=1.58$, adj. P=0.038). These results indicate proteome changes common to all G2019S carriers and associated with G2019S.

Regarding the R1441G proteome, R1441G L2PD vs controls revealed 80 hits (45 down/ 35 up) (**Suppl. Fig. 2**). Of these, 33 proteins (30 down/ 3 up) (44%) overlapped with G2019S L2PD and had the same FC direction, including down-regulation of NDUFB8, a mitochondrial Complex I subunit; PDCD6, a calcium sensor involved vesicle trafficking and apoptosis; RPL11, a component of the 60S ribosomal subunit; and hits such as ATIC, RAB9A, LAMP1, and SLCY. R1441G L2NMCs vs controls showed 5 down-regulated proteins, all common to R1441G L2PD, including NDUFB8 and PDCD6. Between R1441G L2PD and L2NMCs, 2 proteins were up-regulated in R1441G L2PD; ATG3, an E2 ubiquitin-like conjugating enzyme; and MAGT2, which is essential for Golgi protein N-glycosylation. iPD vs controls, despite their larger sample, had only 3 differential hits, all down-regulated and common to L2PD, i.e., SRSF1, an RNA splicing factor; UQCRB, a mitochondrial Complex III subunit; and LAMP1 (**Suppl. Fig. 1 and 4**). Such findings might be related to the clinical heterogeneity of iPD due to diverse genetic and environmental factors. Functionally, proteome changes in G2019S and R1441G L2PD, even iPD, revealed a shared biological enrichment affecting endolysosomal trafficking, proteostasis, and mitochondrial function (**Suppl. Fig. 3**).

Regarding the G2019S phospho-proteome, we found 10,288 phospho-sites mapping to 2,657 proteins in PBMCs. Using the same stringent cut-off from above, G2019S L2PD vs controls displayed a single differential phospho-site, pSer106 RAB12, hyper-phosphorylated in G2019S L2PD ($log_2FC=0.97$; adj. P=0.036) and L2NMCs (log2FC=0.92; adj. P=0.057) (**Fig. 3**). Remarkably, pSer106 RAB12 was shown as a key physiological LRRK2 substrate of higher expression than other RABs in brain from PD models, including pThr73 RAB10.[49,50] G2019S carriers as a whole showed elevated levels of pSer106 RAB12 ($log_2FC=0.95$; adj. P=0.003) and pTyr334 SKAP2 ($log_2FC=1.05$; adj. P=0.003), a protein involved in immune response at peripheral tissues which regulates neural functions at the CNS,[51] including a-synuclein phosphorylation.[52] G2019S L2NMCs vs L2PD showed increased pSer205 MON2 ($log_2FC=1.25$; adj. P=0.05), a regulator of endosome to Golgi trafficking. Lastly, we found no differential hit of G2019S L2NMCs compared to controls. Collectively, these results identify enhanced pSer106 RAB12 levels in a large cohort of G2019S carriers, pinpointing for the first time pSer106 RAB12 as an endogenous biomarker in G2019S PBMCs.

By phospho-proteome analysis of R1441G carriers, R1441G L2PD vs controls showed no hit overpassing the multiple-test adjustment. In addition, R1441G L2NMCs vs controls had 25 differential phospho-sites (20 down/ 5 up), but none included pSer106 RAB12 (**Suppl. Fig. 2**). These findings indicate that enhancement of pSer106 RAB12 phosphorylation is a specific effect in G2019S PBMCs, and suggest distinct phospho-signalling preferences occurring for different pathogenic LRRK2 mutations in G2019S and R1441G patients. Regarding iPD, at the phospho-proteome level, we found no phospho-site change compared to controls (**Suppl. Fig. 4**). However, iPD revealed large phospho-site differences to G2019S L2PD (84 down/ 9 up), including pSer106 RAB12, whose levels were elevated in G2019S L2PD, and also to R1441G L2PD (409 down/ 225 up). Altogether these findings indicate that phospho-protein changes are more prominent in L2PD due to phospho-signalling dysfunction by LRRK2 activating mutations than in iPD, being pSer106 RAB12 a preferred LRRK2 substrate in G2019S PBMCs rather than R1441G or iPD.

By immunoblot we assessed pSer106 RAB12 levels as pSer106 RAB12 / Total RAB12 ratios using >1-year follow-up PBMCs of the G2019S cohort from Clínic-Barcelona (n=48), encompassing G2019S L2PD (n=12), G2019S L2NMCs (n=6), iPD (n=15), and controls (n=15) (**Table 2**). Consistent with DIA-MS data, we found phosphorylation differences across groups

(Kruskal-Wallis P=0.01), with borderline increased pSer106 RAB12 phosphorylation levels in G2019S L2PD (Dunn's adj. P=0.069) and L2NMCs (Dunn's adj. P=0.118) vs controls, and in G2019S carriers as a whole vs controls (Kruskal-Wallis P=0.003; Dunn's adj. P=0.027), but not in iPD (**Fig. 4**, **Suppl. Fig. 5**). By immunoblot[53] we did not observe down-regulation of proteome hits such as RAB9A / GAPDH in G2019S L2PD or iPD (Kruskal-Wallis P=0.08) nor LAMP1 / GAPDH except in iPD (Kruskal-Wallis P=0.03) (Dunn's adj. P=0.046). Lastly, we assessed pSer106 RAB12 response to LRRK2 pharmacological inhibition by Mli-2 in technical replicates from freshly collected PBMCs of an additional set (n=10) of 3 G2019S L2PD, 1 R1441G L2PD, 1 iPD, and 5 controls, treated with Mli-2 (200 nM; 30 min) or DMSO (**Suppl. Fig. 6**). In all subjects, we observed a strong diminishment of pSer106 RAB12 phosphorylation levels after MLi-2 treatment, confirming pSer106 RAB12 as a pharmaco-dynamic readout of LRRK2 inhibition using human PBMCs.

Next, we interrogated phospho-/protein subsets able to classify G2019S carriers and controls. We applied a supported vector machine (SVM) classifier, adjusting for unbalanced group sizes, with 5-fold cross-validation as overfitting control. After recursive feature elimination, we found 510 peptides and 204 phospho-sites subjected as multi-class informative items. By Montecarlo Tree Search (MCTS), we refined combinations of minimal numbers of features yielding maximal balanced accuracy. We found an 18-feature G2019S signature of 15 proteins and 3 phospho-sites (**Fig. 5**), including pSer106 RAB12 among others, e.g., ATIC, RAB9A, LAMP1, NDUFB8, SCLY, or pSer205 MON2, that provided a balanced accuracy to discriminate groups of 0.96 and an area under the curve (AUC) of 1.00 for G2019S L2PD vs controls, and of 0.99 for G2019S L2NMCs. Despite being developed upon G2019S data, the classifier also discriminated R1441G carriers from controls, but not iPD, indicating some common features to R1441G. The top gene ontology term of the 18 features was vesicle transport. We also found a 17-feature G2019S signature involving only proteins (**Suppl. Fig. 7**). These results indicate biological plausibility and 96% disease-prediction ability of the 18-feature phospho-/protein signature to classify G2019S carriers by both mutation and disease status.

Lastly, we interrogated whether deregulated phospho-/proteins were related to disease severity, as assessed by UPDRS-III motor scores. Under a Spearman's Rho>|0.5| and a P<0.05, we found 34 differential proteins (16%) of the 207 hits in G2019S L2PD vs controls with inverse

association with UPDRS-III whereas pSer106 RAB12 and pSer205 MON2 had a direct correlation with motor scoring. Moreover, 10 markers (55%) from the 18-feature G2019S phospho-/protein correlated inversely with UPDRS-III (ATIC, PDCD6, RAB9A, PSMC5, LAMP1, HSD13B10, ARHGAP45, NDUFB8, and SCLY), meanwhile pSer106 RAB12 correlated positively (Rho = 0.49, adj. P = 1.60×10^{-4}) (**Fig. 6**). PDCD6, the top common correlating protein (Rho=-0.75, P=5.51×10^{-10}), participates in vesicle trafficking, mediates mitochondrial cytochrome c release and apoptosis,[54] and has been linked to PD.[55] We also found 65 out of the 80 hits (81%) in R1441G L2PD vs controls correlating with UPDRS-III, both inverse (59%) and positively (41%), several of which were present at the 18-feature G2019S signature (PDCD6, ARHGAP45, NDUFB8, RAB9A, ATIC, SCLY, and LAMP1) whereas others were exclusive for R1441G, e.g., the mitochondrial protein UBQLN4 (Rho=-0.89, P=1.64×10^{-6}) or the cytoskeletal protein PLEC (Rho=0.84, P=3.50×10^{-5}). Although correlation does not mean causality, these results indicate that some phospho-/proteins at the 18-feature G2019S classifier can be related to disease severity therefore holding potential clinical relevance.

DISCUSSION

Following FAIR principles,[27] we employed an interactive tool called Curtain[28] in which the raw and differential analysis data is saved with weblinks which, can be readily explored by non-MS experts. The G2019S L2PD proteome, showed the highest number of changes, approx., 200 proteins, most of which were down-regulated (80%). The G2019S L2NMCs displayed fewer protein differences, around 70, which were also downregulated (85%). There was a strong overlap between proteins that changed in both groups (60%). Comparing G2019S L2PD and G2019S L2NMCs revealed two proteins (RAB9A and SCLY) enhanced in the asymptomatic carriers. Our findings indicate prominent protein deficits mostly associated with LRRK2 mutations such as G2019S, which can begin at G2019S L2NMCs premotor stages[56] and progress in G2019S L2PD.

Metascape gene ontology analysis annotated the protein changes in the G2019S carriers as participating in the endolysosomal biology cycle, involving vesicle trafficking and mitochondrial function. For example, G2019S L2PD showed down-regulation of RAB9A, which controls phagocytosis and lysosomal biology.[57,58] In G2019S carriers we also observed down-regulated levels of LAMP1, a canonical lysosomal marker involved in lysosome biogenesis which supports enhanced LRRK2 activity.[7–9] A previous study also noted that LAMP1 levels were reduced in CSF of L2PD.[59] Our findings are consistent with the current understanding of the LRRK2 pathway indicating that it plays a key role in controlling the endosomal lysosomal pathway.[50,60]

Beyond endolysosomal changes, we also observed changes in proteins involved in ribosomal function, protein homeostasis, and alternative splicing related to G2019S.[61] Thus, ATIC, the top protein down-regulated in G2019S carriers, catalyses the last two steps of mitochondria purine biosynthesis[62,63] and was also linked previously to LRRK2 toxicity.[48] Other deficits included KARS1, a tRNA synthetase; PSMC5, the proteasomal 26S subunit; or SCLY, seleno-cysteine lyase, an enzyme involved in peptide elongation that is also involved in neurodegeneration.[64] Our findings in LRRK2 PMBCs align with studies reporting transcriptional repression of proteostasis regulators in G2019S L2PD,[65] and proteostasis defects in PD substantia nigra.[66]

R1441G L2PD showed 80 differential proteins with 40% shared with G2019S L2PD. Enrichment analysis showed that the functions of the proteins deregulated in the R1441G carriers were similar to G2019S. The R1441G L2PD top protein deficit, NDUFB8, is a subunit of the mitochondrial Complex I (NADH to Ubiquinone oxidoreductase), whose activity is deficient in

PD.[67] R1441G L2PD and L2NMCs displayed few protein differences, notably ATG3, involved in autophagy, and MGAT2, a Golgi glycosyl transferase. Overall the proteomic effects of the G2019S and R1441G LRRK2 mutations in our clinical cohort were quite similar.[68,69]

The iPD proteome, despite being the largest group, displayed only 3 differential hits that were commonly decreased in G2019S and R1441G L2PD. These were LAMP1, which further supports endolysosomal dysfunction occurring in iPD;[60,70] SRSF1, a Serine/Arginine-rich splicing factor; and UQCRB, a mitochondrial Complex III subunit (Ubiquinol-cytochrome c oxidoreductase). Beyond the etiopathological heterogeneity of iPD,[71,72] the relatively fewer protein changes in iPD than G2019S or R1441G L2PD suggest more specific effects of the LRRK2 mutations in dysregulating signal transduction pathways in LRRK2 mutants than in iPD.

Regarding the phospho-proteome, a single hit, pSer106 RAB12, was found to be specifically elevated in the G2019S but not R1441G carriers. Excitingly this phospho-site comprises a key physiological substrate of LRRK2.[2] Overall the roles that RAB12 plays and its phosphorylation by LRRK2 are poorly understood. Phosphorylation of RAB12 is prominent in the brain and observed higher than other RAB substrates such as RAB10 in this organ.[49,50] Other studies showed that RAB12 is located in phagosomes, late endosomes, and lysosomes where it may regulate endosome to trans-Golgi trafficking and exocytosis.[73,74] To our knowledge, this is the first report of hyper-phosphorylated RAB12 in PBMCs from a large cohort of G2019S carriers.

We analysed n=48 follow-up PBMC samples after 1 year by immunoblotting. Despite the lower sample, we found an increase of pSer106 RAB12 in G2019S L2PD and L2NMCs. Previous studies in neutrophils probing for RAB10 but not RAB12 phosphorylation revealed elevated pThr73 RAB10 in R1441G but not G2019S carriers.[19] We also found no RAB10 phosphorylation increase in G2019S and R1441G PBMCs by DIA-MS. Such results in G2019S PBMCs suggest that either RAB12 is a preferred substrate for LRRK2 - indeed, distinct mutation effects cannot be ruled out,[75] and/or that pThr73 RAB10 phosphatases, e.g., PPM1H,[76] dephosphorylate RAB10 more efficient than RAB12. Mechanistic studies on how G2019S and other LRRK2 variants preferentially phosphorylate different RABs in various cell types, using larger cohorts, are warranted. Our study identifies pSer106 RAB12 as an endogenous biomarker in easily accessible PBMCs from carriers of the most prevalent G2019S mutation, either L2PD or L2NMCs.

Upstream of LRRK2, PD cell models showed LRRK2 activation by VPS35/ RAB29 (RAB7L1) binding to a region on the Armadillo (ARM) domain termed 'Site-1'.[22,23] More recently, RAB12 was shown as a key LRRK2 activator that binds to a distinct site at the ARM domain termed 'Site-3'.[24,25] One study showed that RAB12 played a role in recruiting LRRK2 to damaged or stressed lysosomes.[25] These studies suggested that ARM domain Site-1 or Site-3 inhibitors that block RAB binding could serve as novel therapeutic target for allosteric inhibitors of LRRK2 kinase activity.[24] The biological effect of pSer106 RAB12 phosphorylation on LRRK2 regulation has not been well characterised and our results emphasize that additional work is warranted to investigate this.

Downstream of LRRK2, MLi-2 phospho-proteomics identified RAB3A, RAB8A, RAB10, RAB12, RAB29, and RAB43 as LRRK2 substrates.[2,3,20,77] In the clinical setting, only pThr73 RAB10 has been validated as an LRRK2 substrate[19] and exploited as a readout of LRRK2 activity in previous studies,[18] including in LRRK2 inhibitor clinical trials.[12,21] As mentioned above, there has not been a specific way of assessing elevated LRRK2 activity in G2019S carriers due to the lack of effect in pThr73 RAB10 phosphorylation. Monitoring pSer106 RAB12 phosphorylation levels could be especially useful for assessing G2019S selective inhibitors that have been newly developed in clinical studies,[78–81] as these would be expected to preferentially reduce pSer106 RAB12 phosphorylation in patients with heterozygous G2019S mutations.

For G2019S carriers we also identified a signature of 15 proteins and 3 phospho-sites including pSer106 RAB12 that was found to provide a 96% accuracy to discriminate G2019S L2PD, L2NMCs, and controls. Although correlation does not imply causality, signature features such as ATIC, PDCD6, RAB9A, PSMC5, LAMP1, HSD13B10, ARHGAP45, NDUFB8, SCLY, pSer2015 MON2, and pSer106 RAB12 correlated with PD motor severity (UPDRS-III) suggesting that the phospho-signature may be related to PD progression, but further work with larger number of cohorts would be required to assess this clinically.[56] This is the first signature in G2019S PBMCs based on DIA-MS data and complements previous G2019S signatures in blood[82] and urine.[83,84]

Despite the exciting findings, our study has limitations. Inherent variation in humans markedly affects differential protein expression and phosphorylation. Slightly different procedures in PBMCs preparation and storage at different centres can also affect results. To minimise this variation, we undertook MS analysis and data analysis at the same time with blind groups. Third, differential enrichment of phospho-peptides on titanium dioxide beads can result

in further variety. Indeed, we discarded one of the phospho-peptide batches due to not passing quality control. Due to the phospho-peptide enrichment approach used, the detection of phospho-Tyrosines was under-represented. We used a stringent significance cut-off filtering in only hits mapped by at least 2 peptides, and we cannot rule out that other important proteins could have been excluded. Lastly, the number of R1441G carriers, especially L2NMCs, was significantly smaller than G2019S and it was insufficient to assess signatures by machine learning.

In summary, aligning with urine,[84] in PBMCs we found elevated pSer106 RAB12 levels as an endogenous biomarker for G2019S carriers. Given that RAB12 was shown as a key LRRK2 activator in PD models able to increase pThr73 RAB10 levels,[24,25] future studies ought to investigate the effect of pSer106 RAB12 phosphorylation on LRRK2 activation. In line with PD models,[50,85] in human LRRK2 PBMCs we found pSer106 RAB12 as a pharmaco-dynamic readout of MLi-2 LRRK2 inhibition. We also found an 18-feature signature including pSer106 RAB12 with high accuracy in discriminating symptomatic, asymptomatic G2019S carriers, and controls. Future studies need to assess pSer106 RAB12 in other G2019S clinical cohorts, blood cells and CSF, using precise quantitative methods such as reaction monitoring (RM) and ELISA-like assays, to hopefully translate our findings for clinical trials of novel LRRK2 inhibitors.[78–81]

PUBLICLY AVAILABLE DATA

The mass spectrometry proteomics data have been deposited to the ProteomeXchange Consortium via the PRIDE[86] partner repository with the dataset identifiers PXD050865 for the proteome and PXD050944 phospho-proteome analyses. Following FAIR principles,[27] we through the interactive tool called Curtain,[28] raw and differential analysis data is also provided as weblinks which to be readily explored by non-MS experts. Beyond that, programming scripts for data analyses (**Suppl. Material**) (to be provided).

FUNDING

(Please insert only direct funding contributing to this study)

This study was supported by the Michael J. Fox Foundation for Parkinson's Research (MJFF) (#MJFF-000858) to RFS, ME, CM, ES, JI, and JRM.

ACKNOWLEDGEMENTS

We thank the patients and their relatives for their continued and essential collaboration. LDM was funded by the Beatriu-de-Pinòs programme (#BP00176) from the Agència de Gestió d'Ajuts Universitaris i de Recerca (AGAUR). AR was funded by the PFIS programme (#FI21/00104) from the Instituto de Salud Carlos III (ISCIII) co-funded by the European Union. MF was funded by the María-de-Maeztu programme (#MDM-2017-0729) to the Parkinson's disease and Movement Disorders group of the Institut de Neurociències (Universitat de Barcelona). ARC was funded by the EU Next-Generation 2022 Investigo programme from the European Commission (EC) / Agència de Gestió d'Ajuts Universitaris i de Recerca (AGAUR). Research in the Alessi lab were funded by UK Medical Research Council (grant number MC_UU_00018/1) and the pharmaceutical companies supporting the Division of Signal Transduction Therapy Unit (Boehringer Ingelheim, GlaxoSmithKline, and Merck KGaA). RFS was supported by a Miguel Servet grant (#CP19/00048), a FIS grant (#PI20/00659), a PFIS grant (#FI21/00104), and a M-AES grant (#MV22/00041) from the Instituto de Salud Carlos III (ISCIII) co-funded by the European Union. IDIBAPS receives support from the CERCA program of Generalitat de Catalunya.

CONFLICTS OF INTEREST

None of the authors declare conflict of interest.

FINANCIAL DISCLOSURE

None of the authors declare conflict of interest.

REFERENCES

1. Sheng Z, Zhang S, Bustos D, et al. Ser1292 autophosphorylation is an indicator of LRRK2 kinase activity and contributes to the cellular effects of PD mutations. *Sci Transl Med*. 2012;4(164):164ra161. doi:10.1126/scitranslmed.3004485
2. Steger M, Tonelli F, Ito G, et al. Phosphoproteomics reveals that Parkinson's disease kinase LRRK2 regulates a subset of Rab GTPases. *Elife*. 2016;5(JANUARY2016):e12813. doi:10.7554/eLife.12813.001
3. Steger M, Diez F, Dhekne H, et al. Systematic proteomic analysis of LRRK2-mediated Rab GTPase phosphorylation establishes a connection to ciliogenesis. *Elife*. 2017;6:e31012. doi:10.7554/ELIFE.31012
4. Taylor M, Alessi DR. Advances in elucidating the function of leucine-rich repeat protein kinase-2 in normal cells and Parkinson's disease. *Curr Opin Cell Biol*. 2020;63:102-113. doi:10.1016/j.ceb.2020.01.001
5. Zimprich A, Biskup S, Leitner P, et al. Mutations in LRRK2 cause autosomal-dominant parkinsonism with pleomorphic pathology. *Neuron*. 2004;44(4):601-607. doi:S0896627304007202 [pii]10.1016/j.neuron.2004.11.005
6. Paisán-Ruíz C, Jain S, Evans EW, et al. Cloning of the gene containing mutations that cause PARK8-linked Parkinson's disease. *Neuron*. 2004;44(4):595-600. doi:S0896627304006890 [pii]10.1016/j.neuron.2004.10.023
7. Di Maio R, Hoffman EK, Rocha EM, et al. LRRK2 activation in idiopathic Parkinson's disease. *Sci Transl Med*. 2018;10(451):eaar5429. doi:10.1126/scitranslmed.aar5429
8. Fraser KB, Rawlins AB, Clark RG, et al. Ser(P)-1292 LRRK2 in urinary exosomes is elevated in idiopathic Parkinson's disease. *Mov Disord*. 2016;31(10):1543-1550. doi:10.1002/mds.26686
9. Wang X, Negrou E, Maloney MT, et al. Understanding LRRK2 kinase activity in preclinical models and human subjects through quantitative analysis of LRRK2 and pT73 Rab10. *Sci Rep*. 2021;11(1):12900. doi:10.1038/s41598-021-91943-4
10. Healy DG, Falchi M, O'Sullivan SS, et al. Phenotype, genotype, and worldwide genetic penetrance of LRRK2-associated Parkinson's disease: a case-control study. *Lancet Neurol*.

2008;7(7):583-590. doi:10.1016/S1474-4422(08)70117-0

11. Marras C, Alcalay RN, Caspell-Garcia C, et al. Motor and nonmotor heterogeneity of LRRK2-related and idiopathic Parkinson's disease. *Mov Disord*. Published online 2016. doi:10.1002/mds.26614
12. Jennings D, Huntwork-Rodriguez S, Vissers MFJM, et al. LRRK2 Inhibition by BIIB122 in Healthy Participants and Patients with Parkinson's Disease. *Mov Disord*. 2023;38(3):386-398. doi:10.1002/mds.29297
13. Tolosa E, Vila M, Klein C, Rascol O. LRRK2 in Parkinson disease: challenges of clinical trials. *Nat Rev Neurol*. 2020;16(2):97-107. doi:10.1038/s41582-019-0301-2
14. Hentati F, Trinh J, Thompson C, Nosova E, Farrer MJ, Aasly JO. LRRK2 parkinsonism in Tunisia and Norway: A comparative analysis of disease penetrance. *Neurology*. 2014;83(6):568-569. doi:10.1212/WNL.0000000000000675
15. Marder K, Wang Y, Alcalay RN, et al. Age-specific penetrance of LRRK2 G2019S in the Michael J. Fox Ashkenazi Jewish LRRK2 Consortium. *Neurology*. 2015;85(1):89-95. doi:10.1212/WNL.0000000000001708
16. Lee AJ, Wang Y, Alcalay RN, et al. Penetrance estimate of LRRK2 p.G2019S mutation in individuals of non-Ashkenazi Jewish ancestry. *Mov Disord*. 2017;32(10):1432-1438. doi:10.1002/mds.27059
17. Homma Y, Hiragi S, Fukuda M. Rab family of small GTPases: an updated view on their regulation and functions. *FEBS J*. 2021;288(1):36-55. doi:10.1111/febs.15453
18. Karayel, Ö, Tonelli F, Virreira Winter S, et al. Accurate MS-based Rab10 Phosphorylation Stoichiometry Determination as Readout for LRRK2 Activity in Parkinson's Disease. *Mol Cell Proteomics*. 2020;19(9):1546-1560. doi:10.1074/MCP.RA120.002055
19. Fan Y, Nirujogi RS, Garrido A, et al. R1441G but not G2019S mutation enhances LRRK2 mediated Rab10 phosphorylation in human peripheral blood neutrophils. *Acta Neuropathol*. 2021;142(3):475-494. doi:10.1007/s00401-021-02325-z
20. Thirstrup K, Dächsel JC, Oppermann FS, et al. Selective LRRK2 kinase inhibition reduces phosphorylation of endogenous Rab10 and Rab12 in human peripheral mononuclear blood cells. *Sci Rep*. 2017;7(1):10300. doi:10.1038/s41598-017-10501-z

21. Jennings D, Huntwork-Rodriguez S, Henry AG, et al. Preclinical and clinical evaluation of the LRRK2 inhibitor DNL201 for Parkinson's disease. *Sci Transl Med*. 2022;14(648):eabj2658. doi:10.1126/scitranslmed.abj2658
22. Purlyte E, Dhekne HS, Sarhan AR, et al. Rab29 activation of the Parkinson's disease-associated LRRK2 kinase. *EMBO J*. 2018;37(1):1-18. doi:10.15252/embj.201798099
23. Mir R, Tonelli F, Lis P, et al. The Parkinson's disease VPS35[D620N] mutation enhances LRRK2-mediated Rab protein phosphorylation in mouse and human. *Biochem J*. 2018;475(11):1861-1883. doi:10.1042/BCJ20180248
24. Dhekne HS, Tonelli F, Yeshaw WM, et al. Genome-wide screen reveals Rab12 GTPase as a critical activator of Parkinson's disease-linked LRRK2 kinase. *Elife*. 2023;12:e87098. doi:10.7554/elife.87098
25. Wang X, Bondar V V, Davis OB, et al. Rab12 is a regulator of LRRK2 and its activation by damaged lysosomes. *Elife*. 2023;12:12:e87255. doi:10.7554/elife.87255
26. Gustavsson EK, Follett J, Trinh J, et al. RAB32 Ser71Arg in autosomal dominant Parkinson's disease: linkage, association, and functional analyses. *Lancet Neurol*. Published online 10 April 2024. doi:10.1016/S1474-4422(24)00121-2
27. Wilkinson M, Dumontier M, Aalbersberg I. The FAIR Guiding Principles for scientific data management and stewardship. Sci. Data 3 (2016). *Sci data*. 2016;3:1-9. doi:10.1038/sdata.2016.18
28. Phung TK, Berndsen K, Shastry R, et al. CURTAIN-A unique web-based tool for exploration and sharing of MS-based proteomics data. *Proc Natl Acad Sci U S A*. 2024;121(7):e2312676121. doi:10.1073/pnas.2312676121
29. Postuma RB, Berg D, Stern M, et al. MDS clinical diagnostic criteria for Parkinson's disease. *Mov Disord*. 2015;30(12):1591-1601. doi:10.1002/mds.26424
30. Gaig C, Marti MJ, Ezquerra M, Rey MJ, Cardozo A, Tolosa E. G2019S LRRK2 mutation causing Parkinson's disease without Lewy bodies. *J Neurol Neurosurg Psychiatry*. 2007;78(6):626-628. doi:jnnp.2006.107904 [pii]10.1136/jnnp.2006.107904
31. Sierra M, González-Aramburu I, Sánchez-Juan P, et al. High frequency and reduced penetrance of LRRK2 G2019S mutation among Parkinson's disease patients in Cantabria

(Spain). *Mov Disord*. 2011;26(13):2343-2346. doi:10.1002/mds.23965

32. Ruiz-Martínez J, Gorostidi A, Ibañez B, et al. Penetrance in Parkinson's disease related to the LRRK2 R1441G mutation in the Basque country (Spain). *Mov Disord*. 2010;25(14):2340-2345. doi:10.1002/mds.23278
33. Goetz CC. The Unified Parkinson's Disease Rating Scale (UPDRS): Status and recommendations. *Mov Disord*. 2003;18(7):738-750. doi:10.1002/mds.10473
34. Nasreddine ZS, Phillips NA, Bédirian V, et al. The Montreal Cognitive Assessment, MoCA: A brief screening tool for mild cognitive impairment. *J Am Geriatr Soc*. 2005;53(4):695-699. doi:10.1111/j.1532-5415.2005.53221.x
35. Simon-Sanchez J, Marti-Masso JF, Sanchez-Mut J V, et al. Parkinson's disease due to the R1441G mutation in Dardarin: a founder effect in the Basques. *Mov Disord*. 2006;21(11):1954-1959. doi:10.1002/mds.21114
36. Ritchie ME, Phipson B, Wu D, et al. Limma powers differential expression analyses for RNA-sequencing and microarray studies. *Nucleic Acids Res*. 2015;43(7):e47. doi:10.1093/nar/gkv007
37. Virtanen P, Gommers R, Oliphant TE, et al. SciPy 1.0: fundamental algorithms for scientific computing in Python. *Nat Methods*. 2020;17(3):261-272. doi:10.1038/s41592-019-0686-2
38. Seabold S, Perktold J. Statsmodels: Econometric and Statistical Modeling with Python. In: *Proceedings of the 9th Python in Science Conference*. ; 2010:92-96. doi:10.25080/majora-92bf1922-011
39. Bekker-Jensen DB, Bernhardt OM, Hogrebe A, et al. Rapid and site-specific deep phosphoproteome profiling by data-independent acquisition without the need for spectral libraries. *Nat Commun*. 2020;11(1):787. doi:10.1038/s41467-020-14609-1
40. Ogutu JO, Piepho HP, Schulz-Streeck T. A comparison of random forests, boosting and support vector machines for genomic selection. In: *BMC Proceedings*. Vol 5. ; 2011. doi:10.1186/1753-6561-5-S3-S11
41. Chawla N V, Bowyer KW, Hall LO, Kegelmeyer WP. SMOTE: Synthetic minority over-sampling technique. *J Artif Intell Res*. 2002;16:321-357. doi:10.1613/jair.953

42. Brodersen KH, Ong CS, Stephan KE, Buhmann JM. The balanced accuracy and its posterior distribution. In: *Proceedings - International Conference on Pattern Recognition*. ; 2010:3121-3124. doi:10.1109/ICPR.2010.764

43. Pedregosa F, Weiss R, Brucher M, et al. Scikit-learn: Machine Learning in Python. *J Mach Learn Res*. 2011;12:2825-2830. http://jmlr.csail.mit.edu/papers/v12/pedregosa11a.html%5Cnhttp://arxiv.org/abs/1201.0490

44. Van Rossum G, Drake FL, Harris CR, et al. *Python 3 Reference Manual*. Vol 585.; 2009.

45. Chen XW. Gene selection for cancer classification using bootstrapped genetic algorithms and support vector machines. In: *Proceedings of the 2003 IEEE Bioinformatics Conference, CSB 2003*. Vol 46. Springer; 2003:504-505. doi:10.1109/CSB.2003.1227389

46. Gaudel R, Sebag M. Feature selection as a one-player game. In: *ICML 2010 - Proceedings, 27th International Conference on Machine Learning*. ; 2010:359-366.

47. Zhou Y, Zhou B, Pache L, et al. Metascape provides a biologist-oriented resource for the analysis of systems-level datasets. *Nat Commun*. 2019;10(1):1523. doi:10.1038/s41467-019-09234-6

48. Liu Q, Zhu D, Li N, et al. Regulation of LRRK2 mRNA stability by ATIC and its substrate AICAR through ARE -mediated mRNA decay in Parkinson's disease. *EMBO J*. 2023;42(15). doi:10.15252/embj.2022113410

49. Kalogeropulou AF, Freemantle JB, Lis P, Vides EG, Polinski NK, Alessi DR. Endogenous Rab29 does not impact basal or stimulated LRRK2 pathway activity. *Biochem J*. 2020;477(22):4397-4423. doi:10.1042/BCJ20200458

50. Kluss JH, Mazza MC, Li Y, et al. Preclinical modeling of chronic inhibition of the Parkinson's disease associated kinase LRRK2 reveals altered function of the endolysosomal system in vivo. *Mol Neurodegener*. 2021;16(1):17. doi:10.1186/s13024-021-00441-8

51. Ghelman J, Grewing L, Windener F, Albrecht S, Zarbock A, Kuhlmann T. SKAP2 as a new regulator of oligodendroglial migration and myelin sheath formation. *Glia*. 2021;69(11):2699-2716. doi:10.1002/glia.24066

52. Takahashi T, Yamashita H, Nagano Y, et al. Identification and Characterization of a Novel Pyk2/Related Adhesion Focal Tyrosine Kinase-associated Protein That Inhibits α-Synuclein Phosphorylation. *J Biol Chem*. 2003;278(43):42225-42233. doi:10.1074/jbc.M213217200

53. Ayoubi R, Ryan J, Biddle MS, et al. Scaling of an antibody validation procedure enables quantification of antibody performance in major research applications. *Elife*. 2023;12:RP91645. doi:10.1101/2023.06.01.543292

54. Suzuki K, Dashzeveg N, Lu ZG, Taira N, Miki Y, Yoshida K. Programmed cell death 6, a novel p53-responsive gene, targets to the nucleus in the apoptotic response to DNA damage. *Cancer Sci*. 2012;103(10):1788-1794. doi:10.1111/j.1349-7006.2012.02362.x

55. Erekat NS. Apoptosis and its Role in Parkinson's Disease. In: *Parkinson's Disease: Pathogenesis and Clinical Aspects*. Codon Publications; 2018:65-82. doi:10.15586/codonpublications.parkinsonsdisease.2018.ch4

56. Tolosa E, Garrido A, Scholz SW, Poewe W. Challenges in the diagnosis of Parkinson's disease. *Lancet Neurol*. 2021;20(5):385-397. doi:10.1016/S1474-4422(21)00030-2

57. Ao X, Zou L, Wu Y. Regulation of autophagy by the Rab GTPase network. *Cell Death Differ*. 2014;21(3):348-358. doi:10.1038/cdd.2013.187

58. Hirota Y, Yamashita S ichi, Kurihara Y, et al. Mitophagy is primarily due to alternative autophagy and requires the MAPK1 and MAPK14 signaling pathways. *Autophagy*. 2015;11(2):332-343. doi:10.1080/15548627.2015.1023047

59. Hirschberg Y, Valle-Tamayo N, Dols-Icardo O, et al. Proteomic comparison between non-purified cerebrospinal fluid and cerebrospinal fluid-derived extracellular vesicles from patients with Alzheimer's, Parkinson's and Lewy body dementia. *J Extracell Vesicles*. 2023;12(12):12383. doi:10.1002/jev2.12383

60. Vidyadhara DJ, Lee JE, Chandra SS. Role of the endolysosomal system in Parkinson's disease. *J Neurochem*. 2019;150(5):487-506. doi:10.1111/jnc.14820

61. Erb ML, Moore DJ. LRRK2 and the Endolysosomal System in Parkinson's Disease. *J Parkinsons Dis*. 2020;10(4):1271-1291. doi:10.3233/JPD-202138

62. Bulock KG, Peter Beardsley G, Anderson KS. The kinetic mechanism of the human

bifunctional enzyme ATIC (5-amino-4-imidazolecarboxamide ribonucleotide transformylase/inosine 5'-monophosphate cyclohydrolase). A surprising lack of substrate channeling. *J Biol Chem*. 2002;277(25):22168-22174. doi:10.1074/jbc.M111964200

63. Vergis JM, Beardsley GP. Catalytic Mechanism of the Cyclohydrolase Activity of Human Aminoimidazole Carboxamide Ribonucleotide Formyltransferase/Inosine Monophosphate Cyclohydrolase. *Biochemistry*. 2004;43(5):1184-1192. doi:10.1021/bi035139b
64. Byrns CN, Pitts MW, Gilman CA, Hashimoto AC, Berry MJ. Mice lacking selenoprotein P and selenocysteine lyase exhibit severe neurological dysfunction, neurodegeneration, and audiogenic seizures. *J Biol Chem*. 2014;289(14):9662-9674. doi:10.1074/jbc.M113.540682
65. Flinkman D, Hong Y, Gnjatovic J, et al. Regulators of proteostasis are translationally repressed in fibroblasts from patients with sporadic and LRRK2-G2019S Parkinson's disease. *npj Park Dis*. 2023;9(1):20. doi:10.1038/s41531-023-00460-w
66. Jang Y, Pletnikova O, Troncoso JC, et al. Mass Spectrometry–Based Proteomics Analysis of Human Substantia Nigra From Parkinson's Disease Patients Identifies Multiple Pathways Potentially Involved in the Disease. *Mol Cell Proteomics*. 2023;22(1):100452. doi:10.1016/j.mcpro.2022.100452
67. Grünewald A, Rygiel KA, Hepplewhite PD, Morris CM, Picard M, Turnbull DM. Mitochondrial DNA Depletion in Respiratory Chain-Deficient Parkinson Disease Neurons. *Ann Neurol*. 2016;79(3):366-378. doi:10.1002/ana.24571
68. Marchand A, Drouyer M, Sarchione A, Chartier-Harlin MC, Taymans JM. LRRK2 Phosphorylation, More Than an Epiphenomenon. *Front Neurosci*. 2020;14:527. doi:10.3389/fnins.2020.00527
69. Harvey K, Outeiro TF. The role of LRRK2 in cell signalling. *Biochem Soc Trans*. 2018;47(1):197-207. doi:10.1042/BST20180464
70. Rocha EM, Keeney MT, Di Maio R, De Miranda BR, Greenamyre JT. LRRK2 and idiopathic Parkinson's disease. *Trends Neurosci*. 2022;45(3):224-236. doi:10.1016/j.tins.2021.12.002

71. Graham JM, Sagar HJ. A data-driven approach to the study of heterogeneity in idiopathic Parkinson's disease: Identification of three distinct subtypes. *Mov Disord*. 1999;14(1):10-20. doi:10.1002/1531-8257(199901)14:1<10::AID-MDS1005>3.0.CO;2-4

72. Lewis SJG, Foltynie T, Blackwell AD, Bobbins TW, Owen AM, Barker RA. Heterogeneity of Parkinson's disease in the early clinical stages using a data driven approach. *J Neurol Neurosurg Psychiatry*. 2005;76(3):343-348. doi:10.1136/jnnp.2003.033530

73. Bae E-J, Lee S-J. The LRRK2-RAB axis in regulation of vesicle trafficking and α-synuclein propagation. *Biochim Biophys Acta - Mol Basis Dis*. 2020;1866(3):165632. doi:10.1016/j.bbadis.2019.165632

74. Matsui T, Fukuda M. Rab12 regulates mTORC1 activity and autophagy through controlling the degradation of amino-acid transporter PAT4. *EMBO Rep*. 2013;14(5):450-457. doi:10.1038/embor.2013.32

75. Xenias HS, Chen C, Kang S, et al. R1441C and G2019S LRRK2 knockin mice have distinct striatal molecular, physiological, and behavioral alterations. *Commun Biol*. 2022;5(1):1-14. doi:10.1038/s42003-022-04136-8

76. Berndsen K, Lis P, Yeshaw WM, et al. PPM1H phosphatase counteracts LRRK2 signaling by selectively dephosphorylating rab proteins. *Elife*. 2019;8:e50416. doi:10.7554/eLife.50416

77. Liu Z, Bryant N, Kumaran R, et al. LRRK2 phosphorylates membrane-bound Rabs and is activated by GTP-bound Rab7L1 to promote recruitment to the trans-Golgi network. *Hum Mol Genet*. 2018;27(2):385-395. doi:10.1093/hmg/ddx410

78. Lesniak RK, Nichols RJ, Montine TJ. Development of mutation-selective LRRK2 kinase inhibitors as precision medicine for Parkinson's disease and other diseases for which carriers are at increased risk. *Front Neurol*. 2022;13:1016040. doi:10.3389/fneur.2022.1016040

79. Leśniak RK, Nichols RJ, Schonemann M, et al. Discovery of azaspirocyclic 1H-3,4,5-Trisubstitued pyrazoles as novel G2019S-LRRK2 selective kinase inhibitors. *Eur J Med Chem*. 2022;242:114693. doi:10.1016/j.ejmech.2022.114693

80. Lesńiak RK, Nichols RJ, Schonemann M, et al. Discovery of 1H-Pyrazole Biaryl

Sulfonamides as Novel G2019SLRRK2 Kinase Inhibitors. *ACS Med Chem Lett*. 2022;13(6):981-988. doi:10.1021/acsmedchemlett.2c00116

81. Leśniak RK, Nichols RJ, Schonemann M, et al. Discovery of G2019S-Selective Leucine Rich Repeat Protein Kinase 2 inhibitors with in vivo efficacy. *Eur J Med Chem*. 2022;229:114080. doi:10.1016/j.ejmech.2021.114080
82. Garrido A, Santamaría E, Fernández-Irigoyen J, et al. Differential Phospho-Signatures in Blood Cells Identify LRRK2 G2019S Carriers in Parkinson's Disease. *Mov Disord*. 2022;37(5):1004-1015. doi:10.1002/mds.28927
83. Virreira Winter S, Karayel O, Strauss M, et al. Urinary proteome profiling for stratifying patients with familial Parkinson's disease. *EMBO Mol Med*. 2021;13(3):e13257. doi:10.15252/EMMM.202013257
84. Hadisurya M, Li L, Kuwarananchareon K, et al. Quantitative proteomics and phosphoproteomics of urinary extracellular vesicles define putative diagnostic biosignatures for Parkinson's disease. *Commun Med*. 2023;3(1). doi:10.1038/s43856-023-00294-w
85. Kluss JH, Beilina A, Williamson CD, Lewis PA, Cookson MR, Bonet-Ponce L. Lysosomal positioning regulates Rab10 phosphorylation at LRRK2+ lysosomes. *Proc Natl Acad Sci U S A*. 2022;119(43):e2205492119. doi:10.1073/pnas.2205492119
86. Perez-Riverol Y, Bai J, Bandla C, et al. The PRIDE database resources in 2022: A hub for mass spectrometry-based proteomics evidences. *Nucleic Acids Res*. 2022;50(D1):D543-D552. doi:10.1093/nar/gkab1038

FIGURE LEGENDS

Fig. 1. Experimental workflow using PBMCs from a Spanish LRRK2 clinical cohort

(**a**) Peripheral blood mononuclear cells (PBMCs) processing for different applications. 40 ml of blood were drawn from subjects of a LRRK2 clinical cohort from Spain (n=174) encompassing G2019S L2PD patients (n=37), G2019S L2NMCs (n=27), R1441G L2PD patients (n=14), R1441G L2NMCs (n=11), iPD (n=40), and controls (n=45). (**b**) After PBMCs isolation, homogenization, and protein digestion, a total of 3,815 proteins were identified by DIA-MS on an EZ-Exploris 480 mass-spectrometer (Thermo), and 10,288 phospho-sites after phospho-enrichment. For the group differential analysis, we only considered proteins and phospho-sites mapped by ≥2 different peptides (Spetronaut), and with <30% imputation, with a significance cut-off of $\log_2$FC>|0.6| and a multiple testing adjusted P<0.05. Data deconvolution and interactive representation of findings were done using the Curtain / Curtain PTM Tool, and gene ontology was assessed by Metascape. Using machine learning, we identified an 18-feature G2019S phospho-/protein signature able to discriminate G2019S L2PD, G2019S L2NMCs, and controls. By immunoblot, we assessed pSer106 RAB12 / total RAB12 levels in PBMCs from a subject of subjects (n=48) after 1 year of follow-up, including G2019S L2PD (n=12), G2019S L2NMCs (n=6), iPD (n=15) and controls (n=15). Lastly, in freshly isolated PBMCs from a second subset of subjects (n=10) encompassing G2019S L2PD (n=3), R1441G L2PD (n=1), iPD (n=1) and healthy controls (n=5), treated with DMSO or the MLi-2 LRRK2 inhibitor, we performed an LRRK2 kinase assay measuring pSer106 RAB12 / total RAB12 levels.

Fig. 2. Proteome overview and differential analyses in G2019S carriers

(**a**) Barplots showing the numbers of differential proteins in different pairwise comparisons involving G2019S carriers, R1441G carriers, iPD, and controls, with up-regulated proteins in dark grey, and down-regulated in light grey. All cohorts were run in parallel, with balanced study groups per run, blind to the operator, and using 1 quantile normalisation (Limma). The significance cut-off was set at a $\log_2$FC>|0.6| and a multiple testing adjusted P<0.05. (**b**) Volcano plot of the proteome differential analysis in G2019S L2PD vs healthy controls, with Curtain weblinks to access raw and differential analysis data, showing proteins up-regulated in G2019S

L2PD as red dots on the right, and proteins up-regulated in controls (i.e., down-regulated in G2019S L2PD) as red dots on the left (Curtain). A legend colour code applying to all panels is shown at the bottom of the figure, depicting statistically significant hits as red dots. (**c**) Volcano plot of the proteome differential analysis in G2019S carriers as a whole, i.e., L2PD and L2NMCs, vs healthy controls (Curtain). (**d**) Volcano plot showing the proteome differential analysis between G2019S L2NMCs and healthy controls (Curtain). (**e**) Volcano plot representing the proteome comparison between G2019S L2NMCs and G2019S L2PD. A Venn diagram at the bottom of the figure shows the overlap of differential hits in PD-manifesting and non-manifesting G2019S carriers (Curtain).

Fig. 3. Phospho-proteome differential analyses of G2019S carriers

(**a**) Volcano plot of the phospho-proteome differential analysis of G2019S L2PD vs controls, and Curtain weblinks to raw and differential analysis data, showing hyper-phosphorylated proteins in G2019S L2PD as red dots on the right, where a single hit, elevated pSer106 RAB12 levels in G2019S L2PD, emerged (Curtain PTM). A legend colour code shows hits categorisation by statistical significance and applies to all the panels. (**b**) Volcano plot showing phospho-protein hits in G2019S carriers as a whole, PD-manifesting and non-manifesting, compared to controls (Curtain PTM). (**c**) Phospho-proteome differences in G2019S L2NMCs vs controls (Curtain PTM). (**d**) Volcano showing phospho-proteome differences in G2019S L2NMCs vs G2019S L2PD (Curtain PTM). (**e**) QC crude non-imputed (lower bar plot), non-normalised (upper violin plot) mass-spectrometry data from pSer106 RAB12 levels across all study groups showing higher pSer106 phosphorylation levels in G2019S L2PD and G2019S L2NMCs respect to the rest of the groups. The adj. P-values and FC on top of the violin plot correspond to those from the differential analysis. (**f**) A similar analysis to the previous panel with G2019S L2PD and G2019S L2NMCs grouped into a single group of G2019S carriers.

Fig. 4. One-year follow-up of pSer106 RAB12 by immunoblot and MLi-2 response

Immunoblot assessment of pSer106 RAB12 phosphorylation levels in >1-year follow-up PBMC samples from part of the LRRK2 subcohort from Clínic-Barcelona (n=48), including G2019S L2PD

(n=12), G2019S L2NMCs (n=6), iPD (n=15), and controls (n=15). (**a**) Schematic workflow of immunoblot assessment and representative blot from 5 different blots shown in the Supplement. (*) Denotes intergel control. (**b**) dot plots comparing pSer106 RAB12 / Total RAB12 levels obtained by DIA-MS at the entire LRRK2 clinical cohort (n=174) on the left, and by immunoblot of part of the Clínic-Barcelona cohort after 1-year of follow-up (n=48) in G2019S carriers on the right. In each plot, overall intergroup differences were assessed using the Kruskal-Wallis test followed by post-hoc Dunn's test to assess for pSer106 RAB12 / Total RAB12 differences in G2019S carriers. (**c**) Representative immunoblot analysis of pSer106 RAB12 / Total RAB12 and pThr73 RAB10 / Total RAB10 using technical replicates from additional freshly collected PBMCs from one R1441G L2PD, one G2019S L2PD, one iPD and 3 controls (expanded to a total n=10 subjects in the Supplement), treated with DMSO or the MLi-2 LRRK2 inhibitor (200 nM, 30 min), showing a diminishment of pSer106 RAB12 phosphorylation levels after LRRK2 inhibition by MLi-2 treatment.

Fig. 5. Identification of an 18-feature phospho-/protein classifier for G2019S carriers

After comparing the performance of several models, we applied supported vector machine (SVM) learning, adjusted by unbalanced groups using the Synthetic Minority Over-sampling Technique (SMOTE), corrected from overfitting with 5-fold cross-validation, identified cross-group differential proteins and phospho-proteins by ANOVA and Recursive Feature Elimination with Cross-Validation (RFECV), and refined informative combinations to the minimal numbers of features yielding the maximal balanced accuracy by the Montecarlo Tree Search (MCTS) method. (**a**) 18-feature G2019S phospho-/protein best classifier identified in G2019S carriers, both PD-manifesting and non-manifesting subjects, and healthy controls. Red dots indicate individual features correlating with disease severity (UPDRS-III) (See next Figure). (**b**) Relative contribution of the different proteins (n=15) and phospho-sites (n=3), including pSer106 RAB12, from the 18-feature G2019S classifier on the upper bar plot; Metascape gene ontology enrichment analysis of the 18-features G2019S signature lower bar plot. (**c**) Receiver Operating Curve (ROC) analysis of the 18-feature G2019S phospho-/protein signature showing an overall balanced accuracy of 0.957 to discriminate G2019S L2PD, G2019S L2NMCs and controls, specifically with an area under

the curve (AUC) of 1.00 between G2019S L2PD and controls, and 0.99 between G2019S L2NMCs and controls. (**d**) Principal component analysis (PCA) based on the 18-feature G2019S phospho-/protein classifier in G2019S carriers and healthy controls showing distinct group profiles based on LRRK2 mutation and disease status, with G2019S L2NMCs in between G2019S L2PD and controls, consistent with their disease status.

Fig. 6. Association between differential LRRK2 phospho-/proteins and disease severity

Correlation analysis of differential proteins and phospho-proteins (log2FC>|0.6|, adj. P<0.05) and UPDRS-III motor scores from L2PD patients and healthy controls with statistical significance set at a Spearman's correlation coefficient Rho>|0.5| and an FDR multiple-testing adj. P<0.05. (**a**) Correlation plots between differential proteins in G2019S L2PD vs controls on the left, and R1441G L2PD vs controls on the right, showing differential hits correlating with UPDRS-III in red. (**b**) Scatter plot of 10 hits from the 18-feature G2019S phospho-/protein signature correlating with UPDRS-III in G2019S L2PD patients represented as orange dots and healthy controls as blue dots, including PDCD6, ARHGAP45, ATIC, SCLY, PSMC5, NDUFB8, LAMP1, HSD17B10, RAB9A, and pSer106 RAB12.

SUPPLEMENTARY FIGURE LEGENDS

Suppl. Fig. 1 Comparison of proteome hits identified across different groups

Venn diagrams depicting common and specific hits in various groups as compared to healthy controls. (**a**) Differential hits found at various G2019S carrier groups, PD manifesting and non-manifesting, compared to controls. (**b**) Hits from various R1441G carrier groups, symptomatic and asymptomatic, vs controls. (**c**) Common and specific hits were observed in the different PD patient groups, i.e., G2019S L2PD, R1441G L2PD, and iPD. (**d**) Differential hits among L2PD patients carrying either the G2019S or the R1441G mutations, stratified by up and down-regulated hits. (**e**) Differential hits among L2NMCs carrying either the G2019S or the R1441G mutations, as analysed segregated by up and down-regulated hits.

Suppl. Fig. 2. Proteome and phospho-proteome differential analysis of R1441G carriers

Consistently across the study, the significance cut-off for R1441G proteome and phospho-proteome analyses was also set at a $\log_2$FC>|0.6| and a multiple testing adj. P<0.05. A legend colour code applying to all panels is shown at the bottom of the figure, depicting statistically significant hits as red dots. (**a**) Volcano plot of the proteome differential analysis in R1441G L2PD vs healthy controls, with Curtain weblinks to access raw and differential analysis data, showing proteins up-regulated in R1441G L2PD as red dots on the right, and proteins up-regulated in controls (i.e., down-regulated in R1441G L2PD) as red dots on the left (Curtain). (**b**) Volcano plot of the proteome differential analysis in R1441G carriers as a whole, i.e., L2PD and L2NMCs, vs healthy controls (Curtain). (**c**) Volcano plot showing the proteome differential analysis between R1441G L2NMCs and healthy controls (Curtain). (**d**) Volcano plot representing the proteome comparison between R1441G L2NMCs and R1441G L2PD (Curtain). (**e**) Volcano plot of the phospho-proteome differential analysis between R1441G L2PD vs controls (Curtain PTM). (**f**) Volcano plot of the phospho-proteome comparison of R1441G L2NMCs and controls (Curtain PTM).

Suppl. Fig. 3. Proteome functional analysis of G2019S and R1441G patients

Comparative gene ontology (GO) enrichment analysis of the differential proteins observed in G2019S and R1441G L2PD was done in Metascape under a multiple testing adj. P<0.05, here denoted as a dashed red line. (**a**) GO enrichment plot in G2019S L2PD vs controls. (**b**) GO enrichment plot in R1441G L2PD vs controls. Proteome changes related to both mutations showed affection of similar functional terms affecting the endolysosomal pathway (red asterisks), protein homeostasis (green), and mitochondria function (blue).

Suppl. Fig. 4. Proteome and phospho-proteome analysis of iPD compared to L2PD

Curtain weblinks provide access to raw and differential analysis data. The legend colour code shows hits categorisation based on statistical significance and applies to all the panels. (**a**) Volcano plot of the proteome analysis in iPD vs controls showing no differential hit under the statistical cut-off used (Curtain). (**b**) Volcano plot representing protein differences between iPD and G2019S L2PD, showing iPD up-regulated proteins as red dots on the left (Curtain). (**c**) Volcano plot representing protein changes between iPD and R1441G L2PD, with iPD up-regulated proteins as red dots on the left, and iPD down-regulated (i.e., up-regulated in R1441G L2PD) as red dots on the right (**d**) Volcano plot of the phospho-proteome analysis in iPD vs controls showing no differential hit, despite being iPD the groups with larger sample size in the study (Curtain PTM). (**e**) Volcano plot representing phospho-protein differences between iPD and G2019S L2PD, with proteins hyper-phosphorylated in G2019S L2PD as red dots on the right, showing pSer106 RAB12 as top hit, and proteins hyper-phosphorylated in iPD (i.e., hypo-phosphorylated in G2019S L2PD) as red dots on the left (Curtain PTM). (**f**) Similar analysis as in the previous panel, here comparing the phospho-proteome comparison between iPD and R1441G L2PD (Curtain PTM).

Suppl. Fig. 5. Expanded 1-year follow-up of pSer106 RAB12 and other markers by immunoblot

Full immunoblot assessment of pSer106 RAB12 phosphorylation levels, and expression levels of RAB9A and LAMP1, using >1-year follow-up PBMC samples from a subset of the LRRK2 cohort from Clínic-Barcelona (n=48), including G2019S L2PD (n=12), G2019S L2NMCs (n=6), iPD (n=15), and controls (n=15). Dot plots representing normalised levels after the band densitometric analysis for the various studied makers in all subjects studied in duplicates as it follows, pSer106

RAB12 / Total RAB12; RAB9A / GADPH; and LAMP1 / GADPH, all of them double normalised to the same intergel control also measured in duplicates. In each plot, overall intergroup differences were assessed using Kruskal-Wallis test followed by post-hoc Dunn's test under an FDR multiple testing adjusted P<0.05. (*) Denotes intergel control.

Suppl. Fig. 6. Expanded pSer106 RAB12 responsiveness to MLi-2 LRRK2 inhibition

Full immunoblot analysis of pSer106 RAB12 / Total RAB12 and pThr73 RAB10 / Total RAB10 using two technical replicates of PBMC lysates from G2019S L2PD (n=3) and healthy controls (n=3), treated with DMSO or the MLi-2 LRRK2 inhibitor (200 nM, 30 min), showing a diminishment of pSer106 RAB12 phosphorylation levels after LRRK2 inhibition by MLi-2 treatment.

Suppl. Fig. 7. A 17-feature protein classifier for G2019S carriers

To explore alternative classifiers for G2019S carriers and healthy controls, here we applied the same method as described for the 18-feature G2019S phospho-/protein signature, and considered exclusively cross-group differential proteins but not phospho-sites. (**a**) 17-protein G2019S best classifier found in G2019S carriers, symptomatic and asymptomatic, and controls. (**b**) Relative contribution of features from the 17-protein G2019S classifier shown on the upper bar plot; Metascape gene ontology enrichment analysis of the 17-feature G2019S signature displayed on lower bar plot. (**c**) Receiver Operating Curve (ROC) analysis of the 17-protein G2019S signature with a balanced accuracy of 0.963 for discriminating G2019S L2PD, G2019S L2NMCs and controls, with an area under the curve (AUC) of 1.00 between G2019S L2PD and controls, and 0.99 between G2019S L2NMCs and controls. (**d**) Principal component analysis (PCA) based on the 17-protein G2019S classifier displaying different subject profiles of G2019S carriers and healthy controls based on LRRK2 mutation and disease status.

Table 1. Participant clinic-demographics. Data are expressed as a mean ± standard deviation (S.D.) with the number of available subjects/totals in brackets. L2PD = LRRK2-associated PD patients; L2NMC = LRRK2 non-manifesting carriers; iPD = idiopathic PD; C = controls; AAO = age-at-onset; UPDRS-III = Unified Parkinson's Disease Rating Scale; MoCA = Montreal cognitive assessment; LEDD = levodopa equivalent daily dose; "-" = not applicable; NA = not available.

Cohort	N (males/ females)	Age at sampling (years)	PD AAO (years)	Disease duration (years)	UPDRS-III	H&Y	MoCA	LEDD (mg)	Passed COVID-19 (yes/no)
Meta	**174**								
G2019S L2PD	37 (20/17)	63.5±9.1 (37/37)	55.1±10.2 (33/37)	8.4±6.3 (33/37)	16.0±9.7 (34/37)	2.0±0.6 (21/37)	24.3±4.5 (35/37)	635.8± 438.8 (29/39)	4/30 (34/37)
G2019S L2NMC	27 (18/9)	56.7±14.1 (26/27)	-	-	1.0±1.6 (22/27)	-	25.4±6.6 (25/27)	-	6/19 (25/27)
R1441G L2PD	14 (7/7)	67.1±9.5 (14/14)	55.8 ±11.4 (14/14)	12.3± 5.5 (14/14)	19.8±12.0 (14/14)	2.2± 0.9 (13/14)	23.2±5.5 (10/14)	711.5 ± 355.7 (14/14)	4/10 (14/14)
R1441G L2NMC	11 (4/7)	61.1±5.5 (11/11)	-	-	1.2±2.1 (11/11)	-	28.6±2.0 (11/11)	-	1/10 (11/11)
iPD	40 (30/10)	67.3±7.7 (40/40)	62.1±8.5 (40/40)	5.2±4.3 (40/40)	19.7±13.2 (40/40)	2.2±0.6 (31/40)	25.6±3.7 (33/40)	584.7 ± 373.6 (37/40)	1/37 (38/40)
C	45 (18/27)	60.0±10.9 (45/45)	-	-	1.2±2.2 (17/27)	-	27.5±3.2 (27/27)	-	14/30 (44/45)
B - Barcelona	**76**								
G2019S L2PD	16 (7/9)	65.5± 8.3 (16/16)	53.5±11.3 (14/16)	11.4±7.1 (14/16)	13.0± 7.2 (13/16)	2.0± 0.5 (11/16)	25.0±4.3 (14/16)	596.5 ± 269.7 (13/18)	2/12 (14/16)
G2019S L2NMC	11 (7/4)	47.8±15.5 (10/11)	-	-	0.3±0.7 (10/11)	-	28.2±2.0 (10/11)	-	4/5 (9/11)
R1441G L2PD	1 (0/1)	44.0 (1/1)	32.0 (1/1)	12.0 (1/1)	16.0 (1/1)	NA (0/1)	30.0 (1/1)	400 (1/1)	0/1 (1/1)
R1441G L2NMC	3 (2/1)	65.3±1.5 (3/3)	-	-	3.0±3.6 (3/3)	-	29.3±0.6 (3/3)	-	1/2 (3/3)
iPD	20 (16/4)	68.3±7.9 (20/20)	64.3±7.8 (20/20)	4.0 ± 3.0 (20/20)	14.7±4.2 (20/20)	1.9± 0.2 (20/20)	27.2± 3.2 (20/20)	453.8 ± 279.8 (19/20)	1/19 (20/20)
C	25 (9/16)	63.9±10.6 (25/25)	-	-	1.7±2.4 (16/25)	-	27.9±2.1 (25/25)	-	8/17 (25/25)
S - Santander	**55**								
G2019S L2PD	20 (13/0)	61.3±9.0 (20/20)	55.6±9.1 (18/20)	6.1±4.7 (18/20)	18.1±11.0 (20/20)	1.9± 0.6 (9/20)	24.2± 4.6 (20/20)	652.7 ± 562.3 (15/20)	2/17 (19/20)
G2019S L2NMC	15 (11/4)	62.6±10.2 (15/15)	-	-	1.8±1.9 (11/15)	-	23.3±8.1 (14/15)	-	2/13 (15/15)
iPD	10 (6/4)	67.2±7.6 (10/10)	62.0±6.3 (10/10)	5.2±4.0 (10/10)	17.9±8.3 (10/10)	2.5 (1/10)	23±3.5 (10/10)	479.9 ± 220.2 (8/10)	0/8 (8/10)
C	10 (4/6)	56.9±11.1 (10/10)	-	-	NA	-	25.0±3.6 (6/6)	-	1/8 (9/10)
D - Donostia	**43**								
G2019S L2PD	1 (0/1)	78.0 (1/1)	68.0 (1/1)	10.0 (1/1)	15.0 (1/1)	3.0 (1/1)	19.0 (1/1)	893 (1/1)	0/1 (1/1)
G2019S L2NMC	1 (0/1)	58.0 (1/1)	-	-	NA	-	29 (1/1)	-	0/1 (1/1)
R1441G L2PD	13 (7/6)	68.9±7.1 (13/13)	56.5±9.7 (13/13)	12.4±5.7 (13/13)	20.1±12.5 (13/13)	2.2±0.9 (13/13)	22.4±5.2 (9/13)	735.5 ± 358.3 (13/13)	4/9 (13/13)
R1441G L2NMC	8 (2/6)	59.5±5.6 (8/8)	-	-	0.5±0.8 (6/6)	-	28.3±2.3 (6/6)	-	0/8 (8/8)
iPD	10 (8/2)	65.4±7.8 (10/10)	57.9±10.6 (10/10)	7.5±5.9 (10/10)	31.7±20.7 (10/10)	2.7± 0.7 (10/10)	23.7±2.9 (10/10)	917.3 ± 441.8 (10/10)	0/10 (10/10)
C	10 (5/5)	53.5±8.1 (10/10)	-	-	NA	-	29.1±3.9 (5/5)	-	5/5 (10/10)

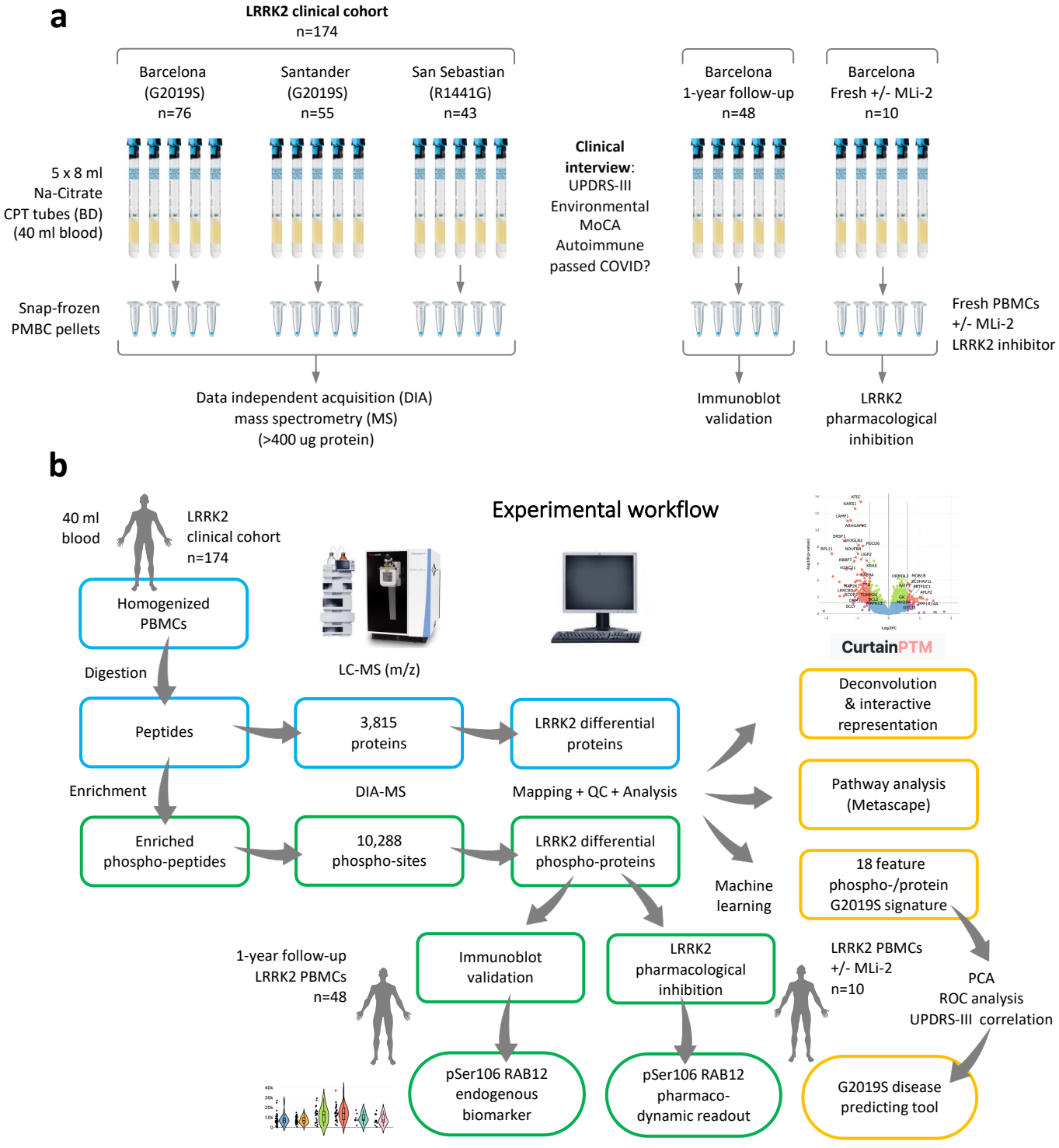

Fig. 1 **Experimental workflow using PBMCs from a Spanish LRRK2 clinical cohort**

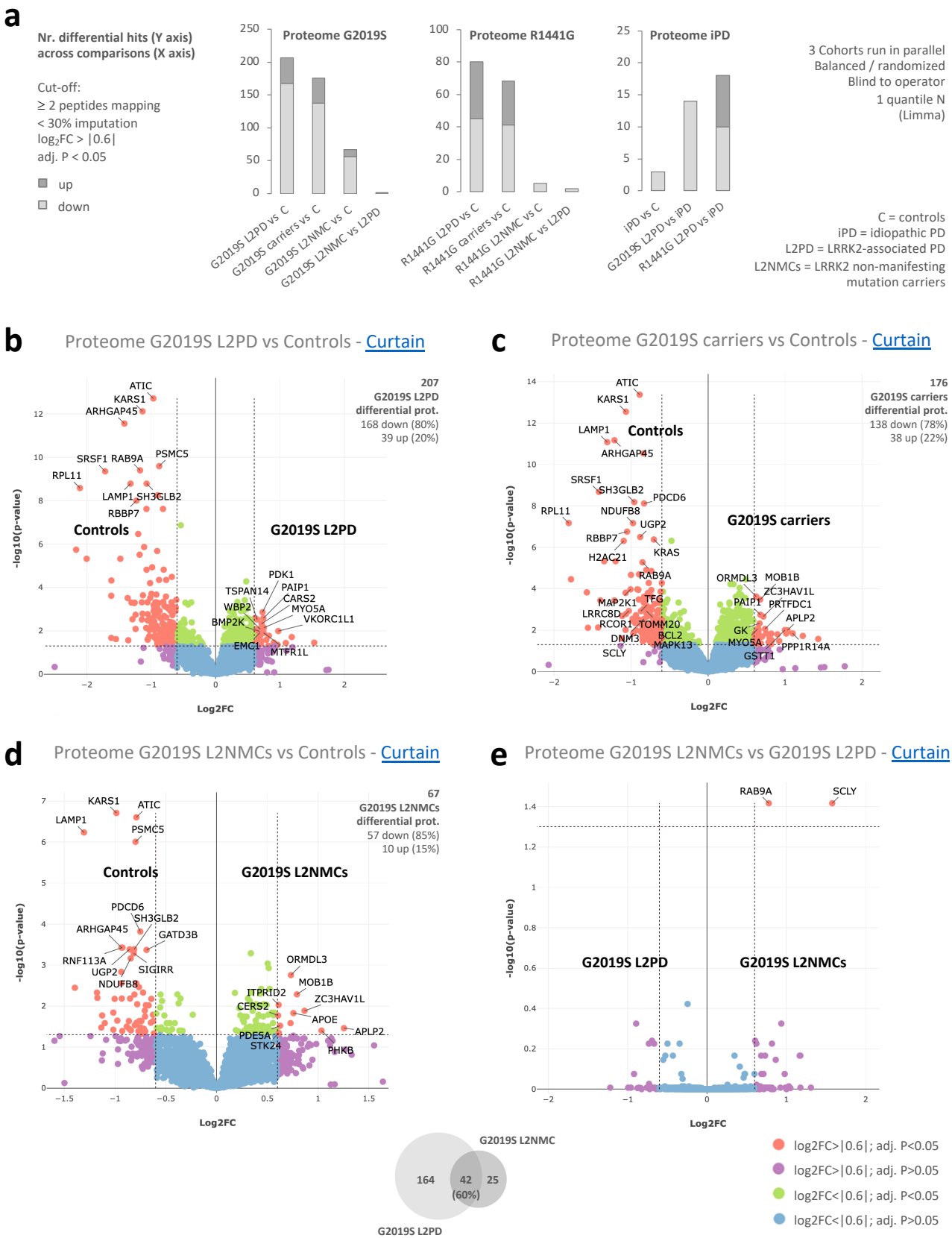

Fig. 2 **Proteome overview and differential analyses in G2019S carriers**

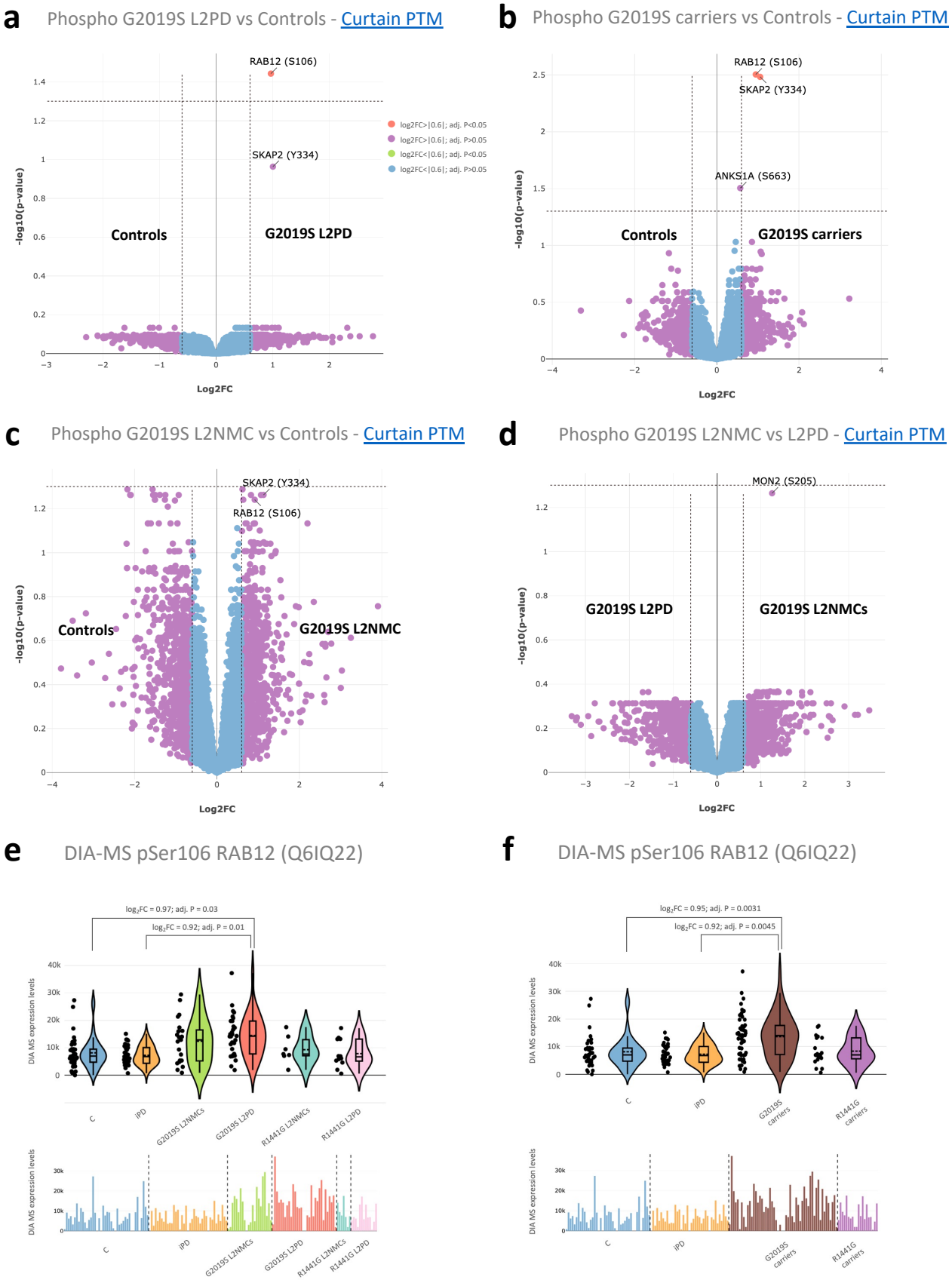

Fig. 3 **Phospho-proteome differential analyses of G2019S carriers**

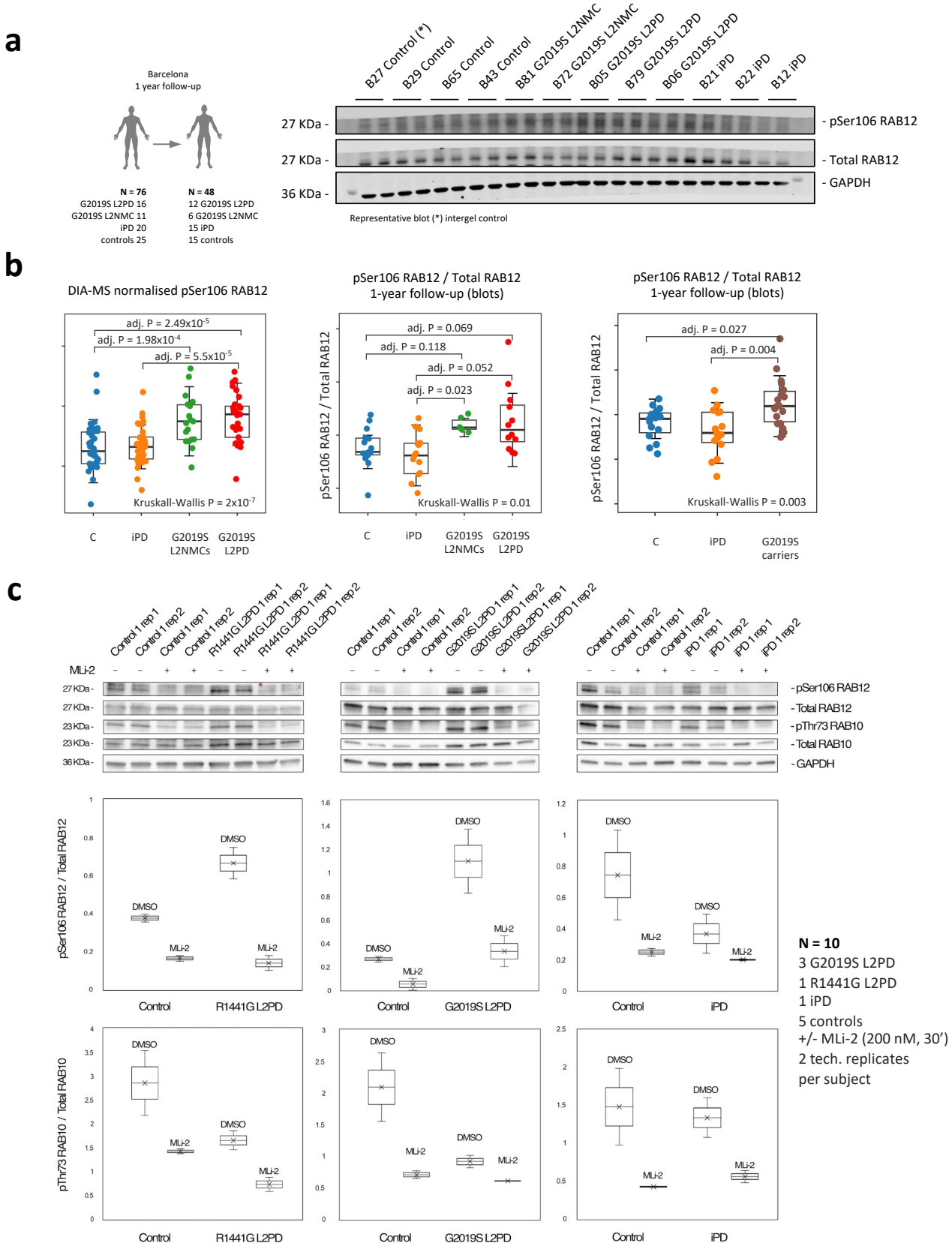

Fig. 4 One-year follow-up of pSer106 RAB12 by immunoblot and MLi-2 response

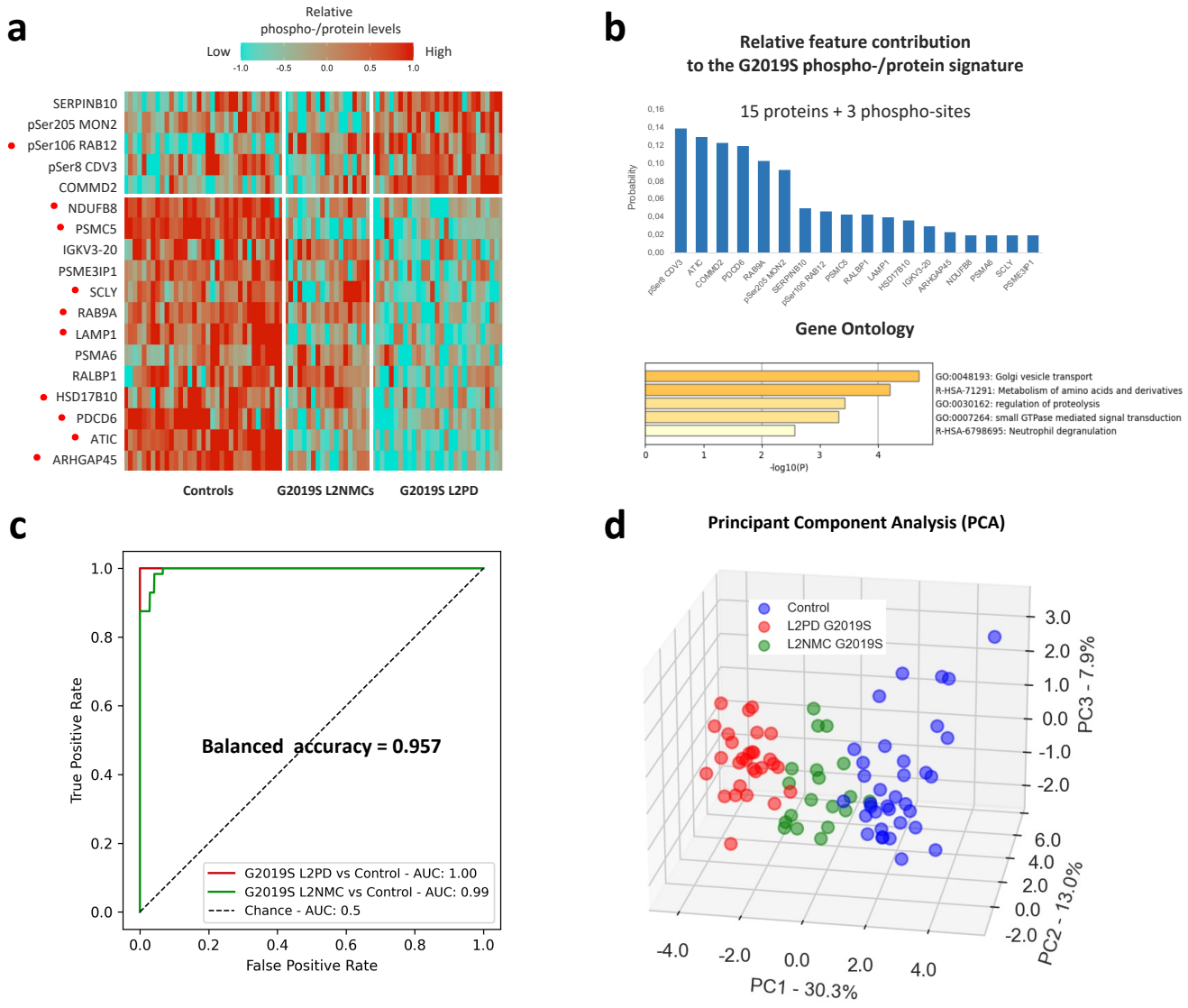

Fig. 5 **Identification of an 18-feature phospho-/protein classifier for G2019S carriers**

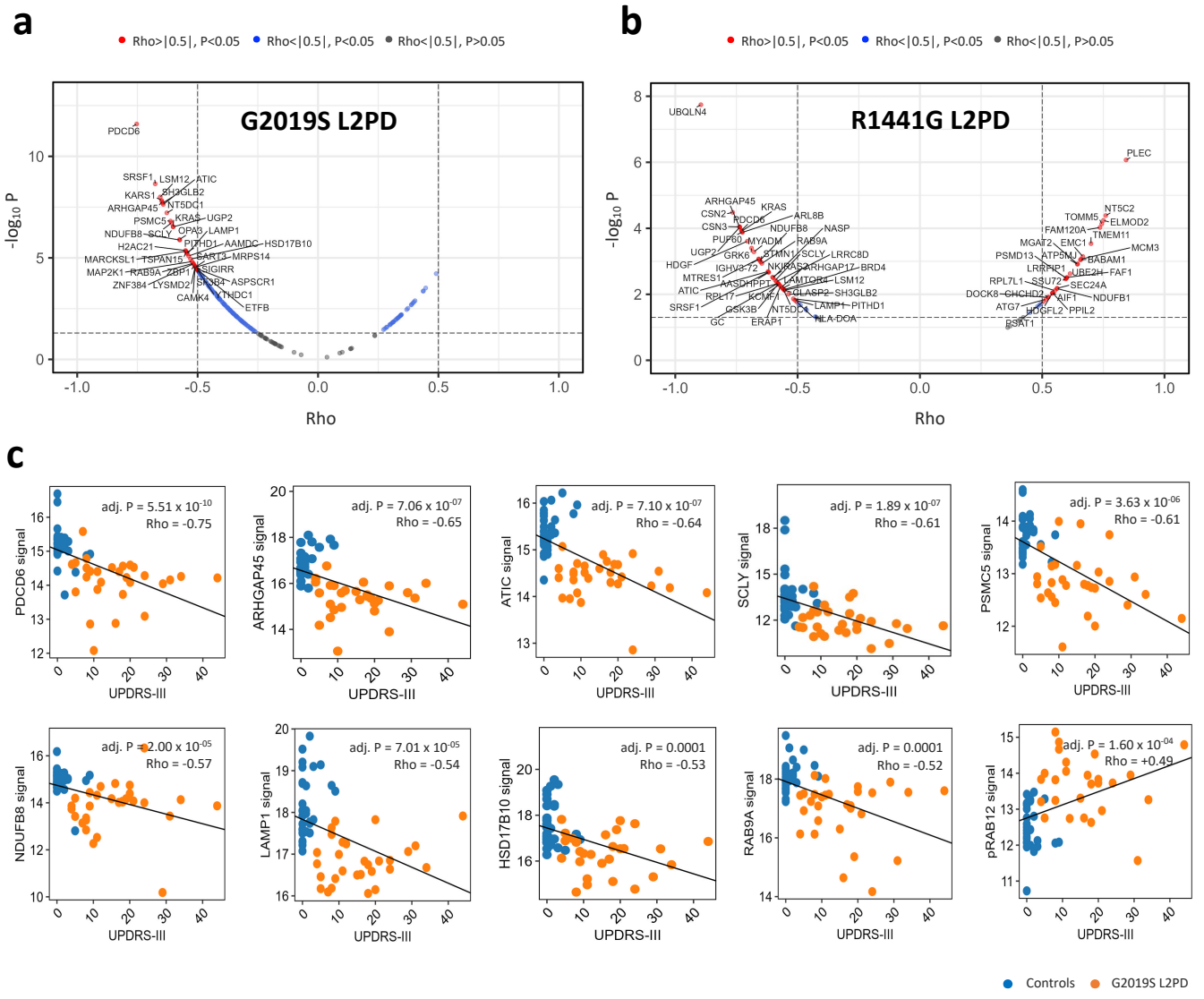

Fig. 6 **Association between differential LRRK2 phospho-/proteins and disease severity**

Suppl. Figs.

a

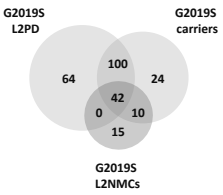

Names	total	elements
G2019S L2NMC G2019S L2PD G2019S carriers	42	HDGF KARS1 MOB1B NR2C2AP CFP SUCLG2 ILK PDCD6 ASH2L SIGIRR PITHD1 RNF113A TOMM20 H2AC21 SRSF1 PSMC5 COG1 NDUFB8 PPIL3 IFITM1 ARHGAP45 YTHDC1 PFDN5 RBBP7 ATIC MT2A UQCRB ZBP1 ELAVL1 LAMP1 METTL9 UGP2 ALOX5AP RPL11 ASPSCR1 ZC3HAV1L STOML2 MAP2K1 SF3B4 LRRC8D SH3GLB2 FANCM
G2019S L2PD G2019S carriers	100	L3HYPDH SMNDC1 DDX3Y GFER PRTFDC1 TPPP3 ASAP2 PHF5A PSPC1 RETN TMA16 BCL2 CASP7 HSD17B10 JPT1 AMPD2 DNM3 PPP1R14A PAIP1 MEN1 PITPNM2 MED22 RCOR1 POLR2J VAV2 CBFB CEBPB HMGN4 ATP8A1 CWF19L1 MARCKSL1 RPL36 LYAR SH3KBP1 ZNF384 GK GOSR1 ARL6IP1 DUSP3 ACAD8 BTF3 ACTG1 GABARAPL2 HLA-DOA RASSF5 MRPS14 SEC11C VKORC1L1 RPL37A 12Å LSM PAAF1 VPS50 CMPK2 KRAS IGKV3-20 ERAP1 PRKCB TCEAL5 NASP CRELD1 ATP5PD HNRNPA2B1 LYSMD2 MMP1 NMT1 STK17B MRPL58 CAMK4 RIN3 PLEKHF1 CAP1 ARL8B TFG SHMT2 5Å LSM PCSK6 MYO5A WASHC3 TAP2 RAB9A ADO GATD1 FUBP1 FNBP4 TSPAN33 AAMDC RGCC CCDC9 AFAP1 FXR1 SAFB MIF4GD UBP1 SCLY EXOC6B NMRAL1 CCT7 EMC1 ACLY OPA3
G2019S L2NMC G2019S carriers	10	ANKS1A HLA-F TXNRD2 PAK1 APLP2 ORMDL3 PHKB UTP18 AP2B1 PGGT1B
G2019S L2PD	64	HNRNPDL RPL23 AASDHPPT SLC4A1 BRD4 NUP54 BRI3BP NT5DC1 TRMT112 AP2M1 GC FTH1 FAF1 LIMA1 RCN1 TOMM5 CLNS1A PDK1 TRABD TSPAN15 ETV6 AGPAT3 MAPK8 MAGED2 RTCA RTF2 DYRK1A PTMS ME1 GSTZ1 BMP2K TBL2 PUF60 CARS2 SCAF4 PRAF2 WBP2 APOL3 NOP14 MTFR1L SRGAP2 SART3 TSPAN14 CTCF RUSF1 ETFB MYH11 NUDT18 IST1 PHKA2 SMYD3 JCHAIN LPA GOLIM4 DDX47 PCTP VRK3 ATP2A3 UBE2J1 PSME3IP1 BCAP29 TRAPPC1 UBQLN4 PRKDC
G2019S L2NMC	15	STK24 RPL17 PCBD2 GATD3B HNRNPD PDE5A MTRES1 RBM8A CDV3 GRK6 UQCRH ITPRID2 APOE CERS2 NDE1
G2019S carriers	24	DMAP1 CSTA GSTT2 SDHC VIL1 SNRNP40 GUCY1B1 LILRA2 S100P MFSD1 HNRNPU ARHGAP17 LRBA MAPK13 APCS DPP9 VPS36 GSTT1 INTS10 IGKC ECM1 UBXN1 IL4I1 ACSBG1

b

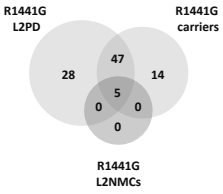

Names	total	elements
R1441G L2NMC R1441G L2PD R1441G carriers	5	HDGF AASDHPPT PDCD6 NDUFB8 MTRES1
R1441G L2PD R1441G carriers	47	ARHGAP17 AIF1 ERAP1 CCAR2 ZNF207 LAMP1 NASP UGP2 GRK6 LAMTOR4 RPL17 ATG7 ILK PITHD1 NT5DC1 JPT1 FAF1 CLASP2 LRRFIP1 IST1 TOMM5 NKIRAS2 NT5C2 RAB9A TSPAN15 PPIL2 SEC24A HDGFL2 ARHGAP45 SSU72 PFDN5 SH3GLB2 LRRC8D ATP5MJ ATIC NDUFC2 SCLY MBOAT7 UBE2H ELMOD2 PSMD13 CALM1 HLA-DOA EMC1 PUF60 PLEC CHCHD2
R1441G L2PD	28	FAM120A LSM12 PSAT1 KRAS MCM3 TBCB NDUFB1 GSK3B MGAT2 BRD4 CTDSP1 TMEM11 KCMF1 GC RPL11 SRSF1 WARS1 ARL8B BABAM1 STMN1 NDUFA11 EIF3L IGHV3-72 RPL7L1 BCL7C MYADM UBQLN4 DOCK8
R1441G carriers	14	TEP1 HNRNPH3 RPL26 RABEP1 UBTF TMEM41B PITPNC1 HNRNPD FUBP1 HMGN4 PNKD KIAA2013 THOC6 HNRNPU

c

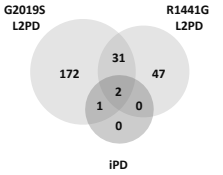

Names	total	elements
G2019S L2PD R1441G L2PD iPD	2	SRSF1 LAMP1
G2019S L2PD iPD	1	UQCRB
G2019S L2PD R1441G L2PD	31	HDGF AASDHPPT ILK BRD4 PDCD6 PITHD1 NT5DC1 JPT1 GC FAF1 TOMM5 NDUFB8 TSPAN15 ARHGAP45 PFDN5 ATIC HLA-DOA PUF60 KRAS ERAP1 NASP UGP2 RPL11 IST1 ARL8B RAB9A LRRC8D SH3GLB2 UBQLN4 SCLY EMC1
G2019S L2PD	172	HNRNPDL KARS1 L3HYPDH SMNDC1 MOB1B DDX3Y GFER PRTFDC1 RPL23 TPPP3 ASAP2 PHF5A NR2C2AP PSPC1 RETN SLC4A1 TMA16 CFP SUCLG2 BCL2 ASH2L NUP54 BRI3BP SIGIRR CASP7 HSD17B10 TRMT112 RNF113A AMPD2 AP2M1 FTH1 TOMM20 DNM3 PPP1R14A LIMA1 H2AC21 RCN1 CLNS1A PSMC5 PAIP1 MEN1 COG1 PPIL3 PITPNM2 PDK1 TRABD ETV6 MED22 RCOR1 POLR2J AGPAT3 VAV2 MAPK8 IFITM1 CBFB CEBPB MAGED2 HMGN4 RTCA RTF2 ATP8A1 CWF19L1 MARCKSL1 RPL36 LYAR SH3KBP1 DYRK1A YTHDC1 PTMS ZNF384 GK RBBP7 MT2A GOSR1 ME1 ARL6IP1 GSTZ1 DUSP3 ACAD8 BTF3 ACTG1 BMP2K GABARAPL2 RASSF5 TBL2 MRPS14 ZBP1 SEC11C VKORC1L1 CARS2 RPL37A SCAF4 12Å LSM PAAF1 VPS50 ELAVL1 CMPK2 PRAF2 WBP2 IGKV3-20 APOL3 NOP14 METTL9 MTFR1L PRKCB TCEAL5 SRGAP2 CRELD1 SART3 ATP5PD TSPAN14 CTCF HNRNPA2B1 RUSF1 LYSMD2 ALOX5AP MMP1 ETFB NMT1 STK17B MYH11 ASPSCR1 MRPL58 NUDT18 CAMK4 RIN3 PHKA2 PLEKHF1 CAP1 SMYD3 TFG SHMT2 5Å LSM PCSK6 JCHAIN MYO5A LPA WASHC3 ZC3HAV1L STOML2 TAP2 GOLIM4 ADO DDX47 PCTP GATD1 MAP2K1 VRK3 ATP2A3 FUBP1 FNBP4 UBE2J1 TSPAN33 AAMDC RGCC CCDC9 SF3B4 AFAP1 FXR1 SAFB MIF4GD PSME3IP1 BCAP29 UBP1 TRAPPC1 PRKDC EXOC6B NMRAL1 CCT7 ACLY OPA3 FANCM
R1441G L2PD	47	PSAT1 CCAR2 ZNF207 MCM3 TBCB NDUFB1 LAMTOR4 RPL17 WARS1 NT5C2 IGHV3-72 PPIL2 SEC24A ATP5MJ UBE2H ELMOD2 PSMD13 CALM1 MTRES1 CHCHD2 PLEC ARHGAP17 FAM120A AIF1 LSM12 GSK3B GRK6 MGAT2 ATG7 CTDSP1 TMEM11 KCMF1 CLASP2 LRRFIP1 NKIRAS2 BABAM1 STMN1 EIF3L NDUFA11 RPL7L1 HDGFL2 BCL7C SSU72 MYADM NDUFC2 DOCK8 MBOAT7

d

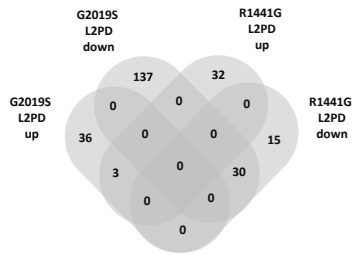

Names	total	elements
G2019S L2PD up R1441G L2PD up	3	FAF1 TOMM5 EMC1
G2019S L2PD down R1441G L2PD down	30	HDGF AASDHPPT ILK BRD4 PDCD6 PITHD1 NT5DC1 JPT1 GC SRSF1 NDUFB8 TSPAN15 ARHGAP45 PFDN5 ATIC HLA-DOA PUF60 KRAS ERAP1 LAMP1 NASP UGP2 RPL11 IST1 ARL8B RAB9A LRRC8D SH3GLB2 UBQLN4 SCLY
G2019S L2PD up	36	L3HYPDH MOB1B PRTFDC1 AP2M1 PPP1R14A RCN1 PAIP1 MEN1 PITPNM2 PDK1 TRABD AGPAT3 RTCA ATP8A1 GK ME1 BMP2K VKORC1L1 CARS2 PAAF1 WBP2 MTFR1L PRKCB TSPAN14 RUSF1 MYH11 CAP1 SMYD3 PCSK6 MYO5A ZC3HAV1L PCTP ATP2A3 RGCC SAFB TRAPPC1
G2019S L2PD down	137	HNRNPDL KARS1 SMNDC1 DDX3Y GFER RPL23 TPPP3 ASAP2 PHF5A NR2C2AP PSPC1 RETN SLC4A1 TMA16 CFP SUCLG2 BCL2 ASH2L NUP54 BRI3BP SIGIRR CASP7 HSD17B10 TRMT112 RNF113A AMPD2 FTH1 TOMM20 DNM3 LIMA1 H2AC21 CLNS1A PSMC5 COG1 PPIL3 ETV6 MED22 RCOR1 POLR2J VAV2 MAPK8 IFITM1 CBFB CEBPB MAGED2 HMGN4 RTF2 CWF19L1 MARCKSL1 RPL36 LYAR SH3KBP1 DYRK1A YTHDC1 PTMS ZNF384 RBBP7 MT2A GOSR1 ARL6IP1 GSTZ1 DUSP3 ACAD8 BTF3 UQCRB ACTG1 GABARAPL2 RASSF5 TBL2 MRPS14 ZBP1 SEC11C RPL37A SCAF4 12Å LSM VPS50 ELAVL1 CMPK2 PRAF2 IGKV3-20 APOL3 NOP14 METTL9 TCEAL5 SRGAP2 CRELD1 SART3 ATP5PD CTCF HNRNPA2B1 LYSMD2 ALOX5AP MMP1 ETFB NMT1 STK17B ASPSCR1 MRPL58 CAMK4 RIN3 NUDT18 PHKA2 PLEKHF1 TFG SHMT2 5Å LSM JCHAIN LPA WASHC3 STOML2 TAP2 GOLIM4 ADO DDX47 GATD1 MAP2K1 VRK3 FUBP1 FNBP4 UBE2J1 TSPAN33 AAMDC CCDC9 SF3B4 AFAP1 FXR1 MIF4GD PSME3IP1 BCAP29 UBP1 PRKDC EXOC6B NMRAL1 CCT7 ACLY OPA3 FANCM
R1441G L2PD up	32	PSAT1 CCAR2 ZNF207 MCM3 TBCB NDUFB1 NT5C2 PPIL2 SEC24A ATP5MJ UBE2H ELMOD2 PSMD13 CALM1 CHCHD2 PLEC FAM120A AIF1 MGAT2 ATG7 TMEM11 LRRFIP1 BABAM1 EIF3L NDUFA11 RPL7L1 HDGFL2 BCL7C SSU72 NDUFC2 DOCK8 MBOAT7
R1441G L2PD down	15	LAMTOR4 RPL17 WARS1 IGHV3-72 MTRES1 ARHGAP17 LSM12 GSK3B GRK6 CTDSP1 KCMF1 CLASP2 NKIRAS2 STMN1 MYADM

e

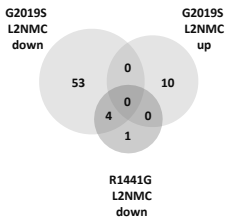

Names	total	elements
G2019S L2NMC down R1441G L2NMC down	4	HDGF PDCD6 NDUFB8 MTRES1
G2019S L2NMC up	10	MOB1B STK24 ORMDL3 PHKB ZC3HAV1L PDE5A ITPRID2 APOE CERS2 APLP2
G2019S L2NMC down	53	KARS1 ANKS1A ELAVL1 NR2C2AP METTL9 LAMP1 UGP2 GRK6 CFP RPL17 SUCLG2 ILK HLA-F ASH2L TXNRD2 SIGIRR PITHD1 UTP18 PAK1 RNF113A ALOX5AP TOMM20 RPL11 ASPSCR1 PCBD2 H2AC21 SRSF1 PSMC5 GATD3B COG1 UQCRH PPIL3 HNRNPD STOML2 MAP2K1 IFITM1 ARHGAP45 YTHDC1 SF3B4 PFDN5 LRRC8D SH3GLB2 RBBP7 ATIC MT2A AP2B1 UQCRB RBM8A PGGT1B CDV3 FANCM ZBP1 NDE1
R1441G L2NMC down	1	AASDHPPT

Suppl. Fig. 1 **Comparison of proteome hits identified across different groups**

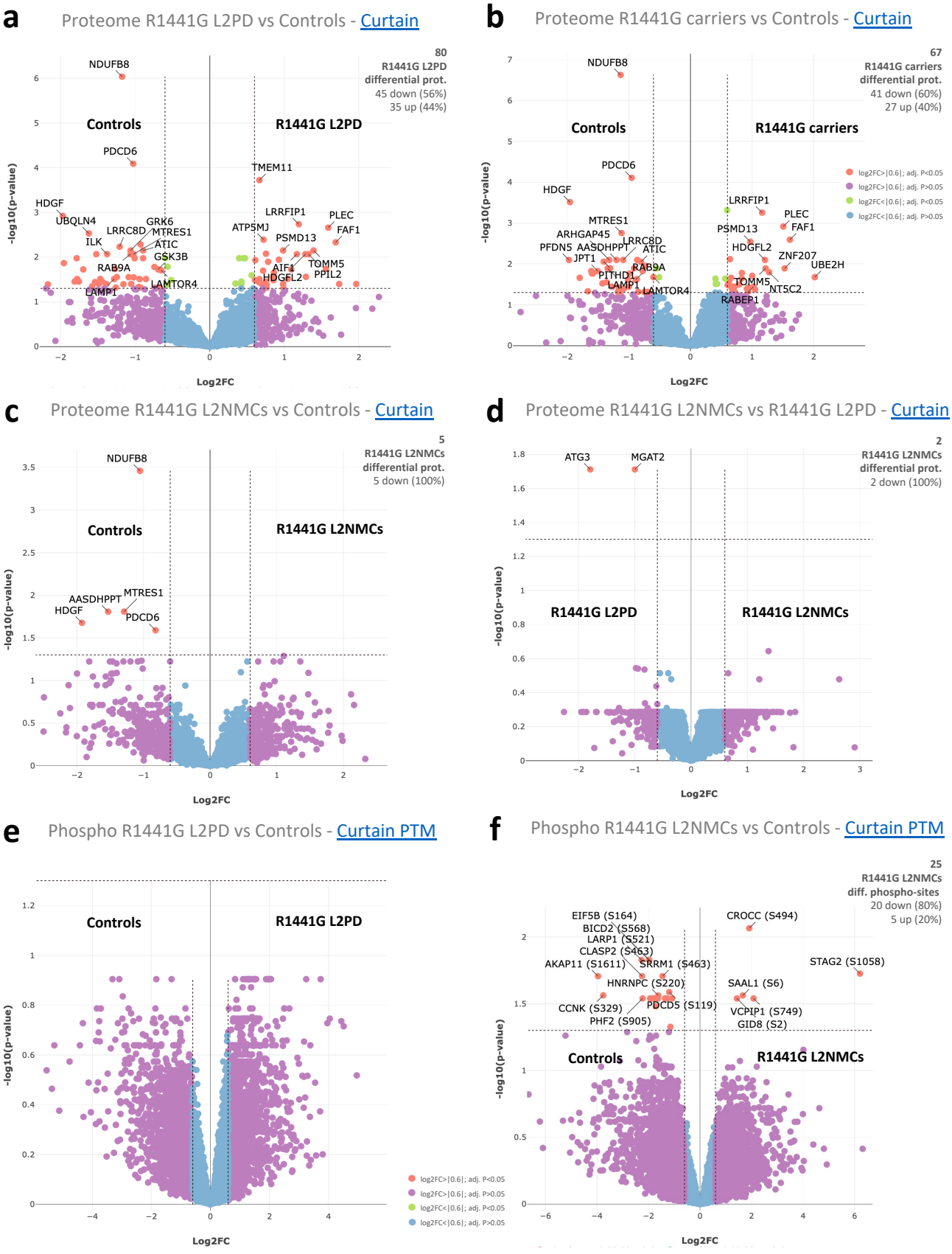

Suppl. Fig. 2 **Proteome and phospho-proteome differential analysis of R1441G carriers**

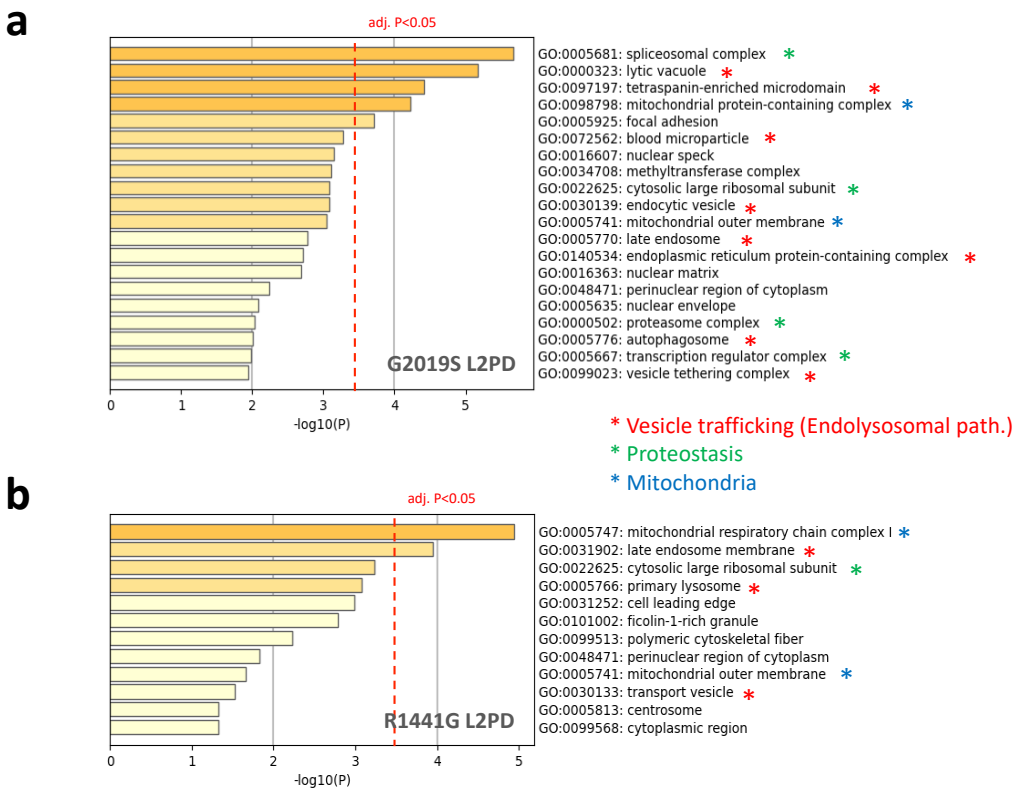

Suppl. Fig. 3 **Proteome functional analysis of G2019S and R1441G patients**

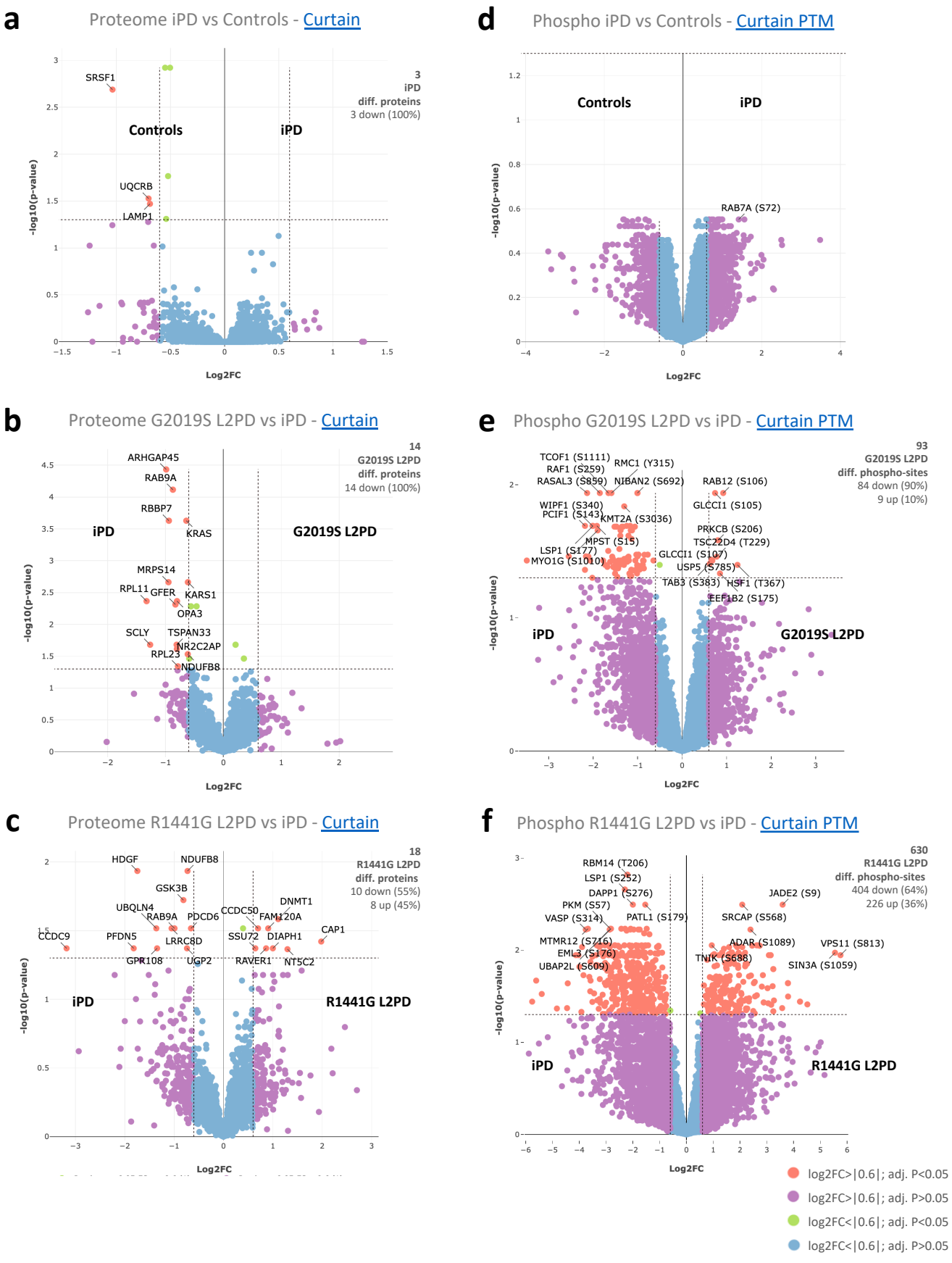

Suppl. Fig. 4 **Proteome and phospho-proteome analysis of iPD compared to L2PD**

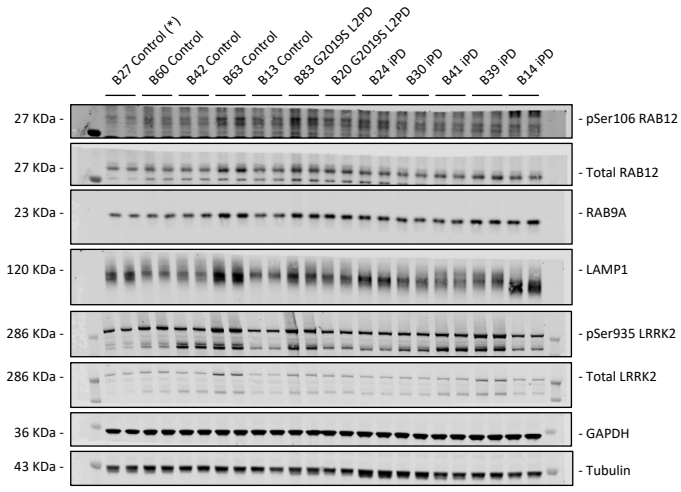

Gel 1

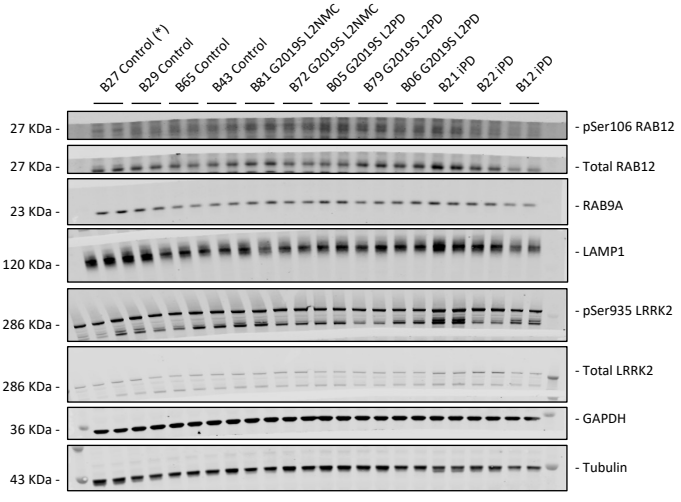

Gel 2

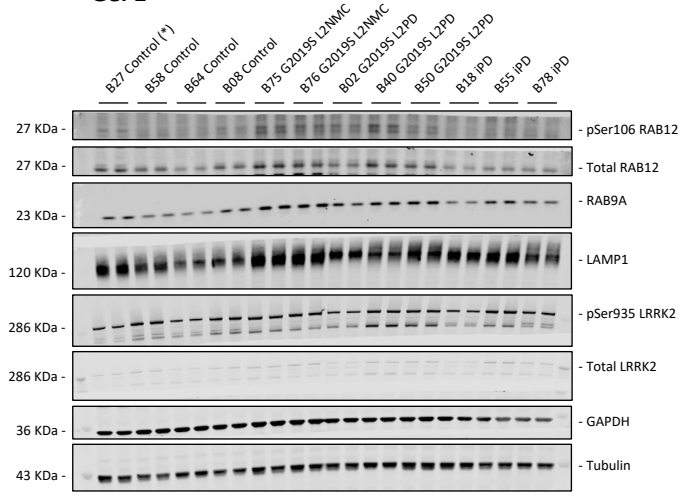

Gel 3

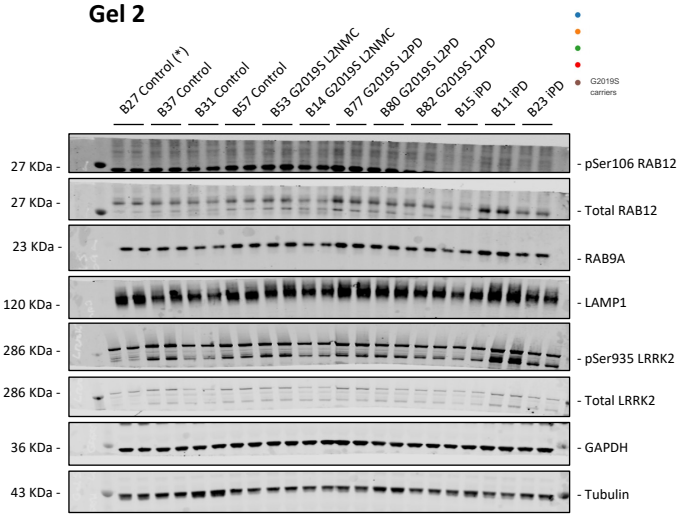

Gel 4

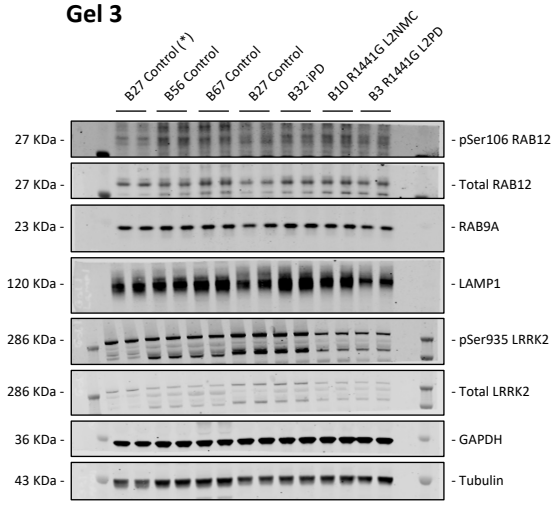

Gel 5

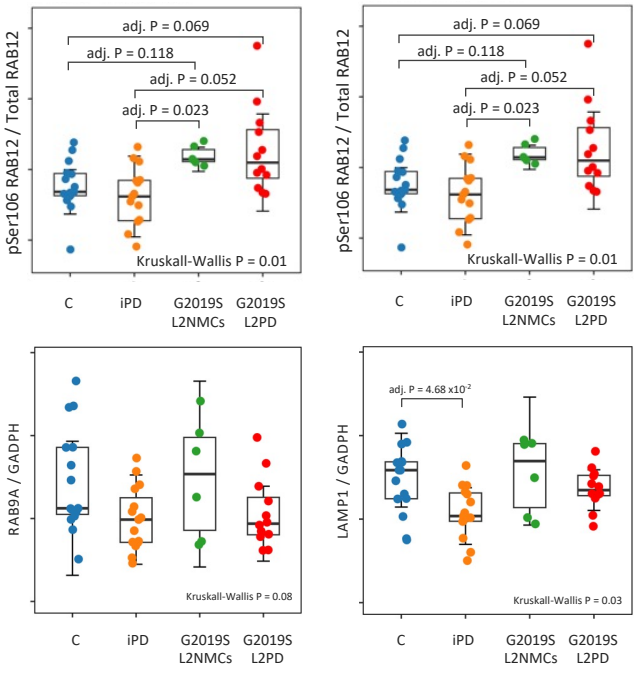

Suppl. Fig. 5 **Expanded 1-year follow-up of pSer106 RAB12 and other markers by immunoblot**

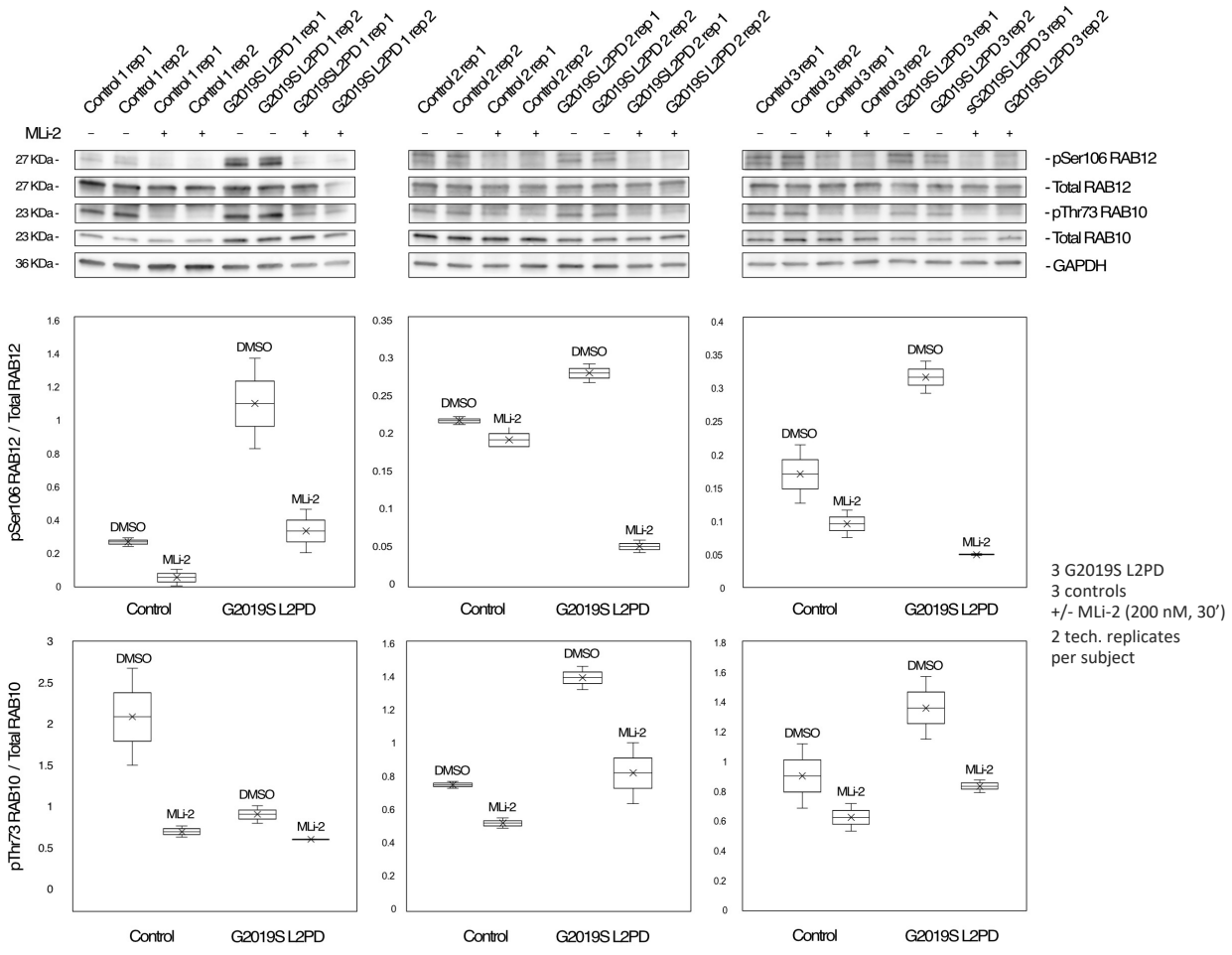

Suppl. Fig. 6 **Expanded pSer106 RAB12 responsiveness to MLi-2 LRRK2 inhibition**

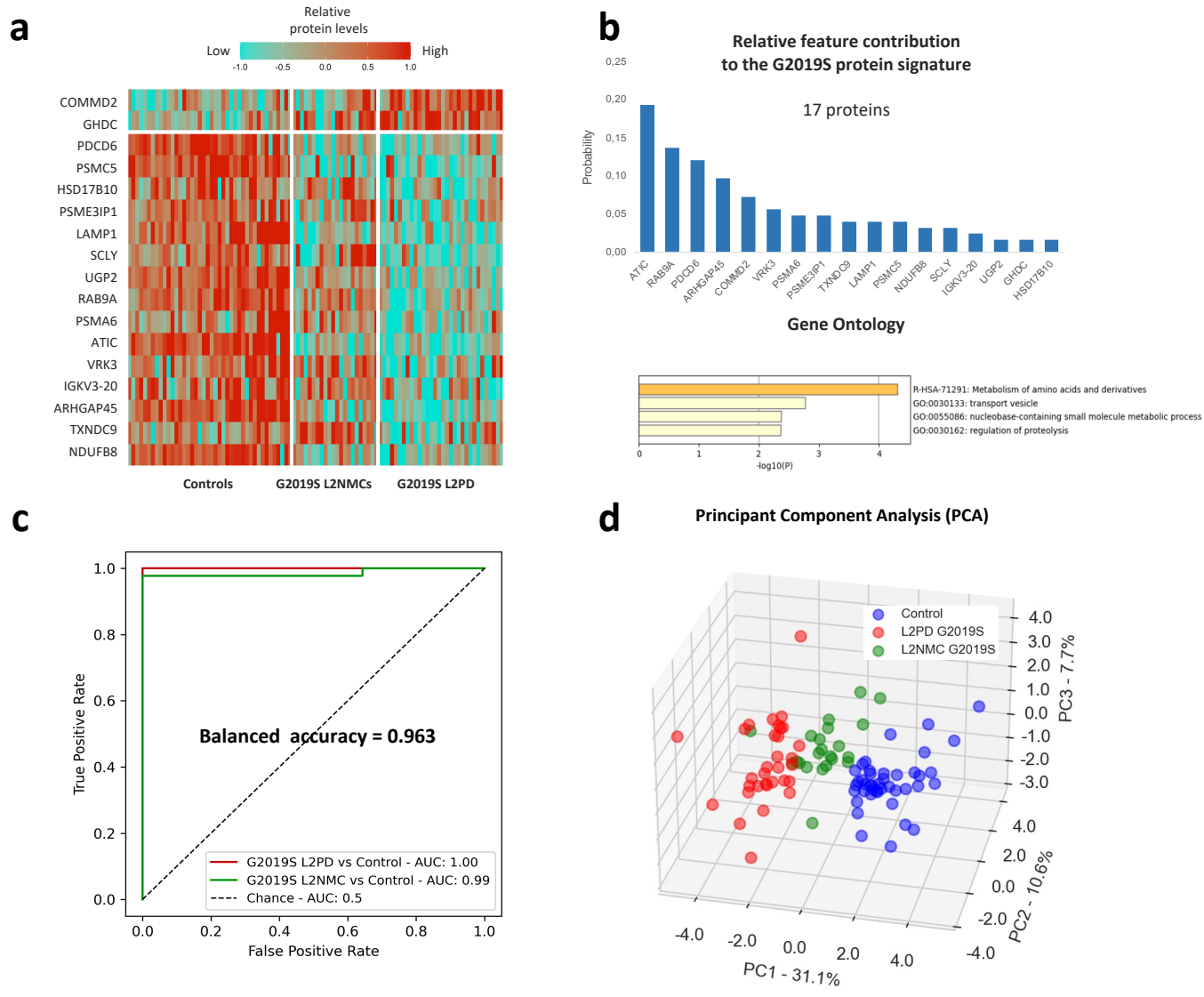

Suppl. Fig. 7 **A 17-feature protein classifier for G2019S carriers**